J. Fluid Mech. (1998), *vol.* 376, *pp.* 183–219. Printed in the United Kingdom

© 1998 Cambridge University Press

Experimental study of vortex breakdown in swirling jets

By PAUL BILLANT[1,2], JEAN-MARC CHOMAZ[1] AND PATRICK HUERRE[1]

[1]LadHyX, CNRS–UMR 156, École Polytechnique, F–91128 Palaiseau Cedex, France
[2]Météo–France CNRM Toulouse, 42 avenue Coriolis, F–31057 Toulouse, France

(Received 15 April 1997 and in revised form 1 July 1998)

The goal of this study is to characterize the various breakdown states taking place in a swirling water jet as the swirl ratio S and Reynolds number Re are varied. A pressure-driven water jet discharges into a large tank, swirl being imparted by means of a motor which sets into rotation a honeycomb within a settling chamber. The experiments are conducted for two distinct jet diameters by varying the swirl ratio S while maintaining the Reynolds number Re fixed in the range $300 < Re < 1200$. Breakdown is observed to occur when S reaches a well defined threshold $Sc \approx 1.3$–1.4 which is independent of Re and nozzle diameter used. This critical value is found to be in good agreement with a simple criterion derived in the same spirit as the first stage of Escudier & Keller's (1983) theory. Four distinct forms of vortex breakdown are identified: the well documented bubble state, a new cone configuration in which the vortex takes the form of an open conical sheet, and two associated asymmetric bubble and asymmetric cone states, which are only observed at large Reynolds numbers. The two latter configurations differ from the former by the precession of the stagnation point around the jet axis in a co-rotating direction with respect to the upstream vortex flow. The two flow configurations, bubble or cone, are observed to coexist above the threshold Sc at the same values of the Reynolds number Re and swirl parameter S. The selection of breakdown state is extremely sensitive to small temperature inhomogeneities present in the apparatus. When S reaches Sc, breakdown gradually sets in, a stagnation point appearing in the downstream turbulent region of the flow and slowly moving upstream until it reaches an equilibrium location. In an intermediate range of Reynolds numbers, the breakdown threshold displays hysteresis lying in the ability of the breakdown state to remain stable for $S < Sc$ once it has taken place. Below the onset of breakdown, i.e. when $0 < S < Sc$, the swirling jet is highly asymmetric and takes the shape of a steady helix. By contrast above breakdown onset, cross-section visualizations indicate that the cone and the bubble are axisymmetric. The cone is observed to undergo slow oscillations induced by secondary recirculating motions that are independent of confinement effects.

1. Introduction

The objective of the present experimental study is to characterize the vortex breakdown phenomenon that may arise in a swirling water jet discharging into a large tank. Distinct breakdown states are identified in the form of a bubble, a cone, an asymmetric bubble and an asymmetric cone and a quantitative comparison is presented between the prediction of a simple breakdown criterion and experimental

https://doi.org/10.1017/S0022112098002870 Published online by Cambridge University Press

observations. The main features of vortex breakdown, i.e. the presence of hysteresis, azimuthal symmetry or lack thereof and secondary motions of the breakdown states are documented and analysed.

Vortex breakdown is a remarkable feature affecting geophysical flows such as tornadoes or man-made flows such as tip vortices produced over delta wings. These vortical flows are typically characterized by the presence of an appreciable axial velocity superimposed upon the rotational motion. When the ratio of azimuthal to axial velocity exceeds a certain level of order unity, 'vortex breakdown' takes place, i.e. the vortex core abruptly widens into a new stable coherent structure. Although various forms of vortex breakdown have been identified, they all share as a common and predominant feature an abrupt deceleration of the flow near the axis leading to the formation of a stagnation point, as if a solid obstacle had been introduced into the flow. Experiments on vortex breakdown have been carried out over delta wings (Peckham & Atkinson 1957; Lambourne & Bryer 1961), in confined tubes (Harvey 1962; Sarpkaya 1971, 1974, 1995; Faler & Leibovich 1977, 1978; Garg & Leibovich, 1979; Escudier & Zehnder 1982; Brücker & Althaus 1992; Brücker 1993; Brücker & Althaus 1995), in a cylindrical container with a rotating endwall (Escudier 1984), in a tornado generator (Khoo *et al*. 1997) or in a free swirling air jet (Farokhi, Taghavi & Rice 1988; Panda & McLaughlin 1994).

The two predominant breakdown configurations, namely the bubble and the spiral, were first identified by Lambourne & Bryer (1961) in the tip vortices generated by flow over delta wings. The distinction between these two states is mainly based upon flow visualizations where dye is introduced on the vortex axis. In the case of a bubble, the filament of dye spreads symmetrically to delineate the stagnant region. By contrast, in the spiral type breakdown, the dye filament is deformed into a spiral configuration. It is then inferred that an oscillatory disturbance sets successive particles on different paths over the stagnant region.

A major drawback of the delta wing experiments is that axial and azimuthal velocities cannot be varied independently, so that most of subsequent experiments on vortex breakdown have been made in the more controlled situation of straight or slightly diverging confined tubes with swirl imparted by upstream guidevanes. In this type of experimental arrangement, Sarpkaya (1971) observed in addition to the bubble and the spiral, a third state: the double helix. As pointed out by Leibovich (1978), this flow configuration does not exhibit a stagnation point and consequently it does not, strictly speaking, qualify as a breakdown state. With a similar experimental set-up, Faler & Leibovich (1977) have identified up to six distinct modes of vortex core disruption, among which four are breakdown states corresponding to various configurations of bubbles or spirals. The two new distinct breakdown states isolated by these authors correspond to a bubble which is flattened in a steady preferred plane (type 4) and a state (type 3) sharing the characteristics of both the spiral breakdown and the flattened bubble.

The confinement imposed by the tube is found to critically control the occurrence of breakdown: Sarpkaya (1974), Escudier & Zehnder (1982) and Althaus, Brücker & Weimer (1995) by taking tubes with various angles of divergence that create an adverse pressure gradient, have demonstrated that breakdown occurs at lower Reynolds number when the pipe flare angle is increased, a feature which effectively adds another control parameter to the problem. However, the various forms of breakdown states do not seem to be very sensitive to confinement effects: Khoo *et al*. (1997) have observed and identified the same six modes of vortex core disruption in their unconfined tornado generator as in the confined tube configuration of Faler & Leibovich (1977).

https://doi.org/10.1017/S0022112098002870 Published online by Cambridge University Press

In free swirling jets, experimental investigations of vortex breakdown have been conducted at high Reynolds numbers and have mainly concentrated on a detailed documentation of velocity distributions and associated turbulence fluctuations (see, for instance, Farokhi *et al*. 1988; Panda & McLaughlin 1994).

Quantitative measurements by laser Doppler anemometry (Faler & Leibovich 1977; Uchida, Nakamura & Oshawa 1985) and particle tracking velocimetry (Brücker & Althaus 1992) have provided a detailed picture of the internal structure of the bubble. Much of the long–inferred topology of spiral breakdown has recently been revealed by the instantaneous particle tracking measurements of Brücker (1993) which actually indicate a strong similarity with the bubble except that the stagnation point is not located on the vortex axis but precesses around it.

According to previous investigations, vortex breakdown is known to exhibit widespread hysteresis and bistability behaviour. The classic photograph of Lambourne & Bryer (1961) which simultaneously displays on each side of a delta wing, i.e. for the same imposed flow conditions, the spiral and the bubble, constitutes a striking example of bistability. In confined tubes, Sarpkaya (1971) and Faler & Leibovich (1977) also identified flow regimes where the spiral and the bubble were highly unstable and the flow configuration changed over time from one to the other. The latter authors and Escudier & Zehnder (1982) have reported random and unpredictable transitions between different kinds of bubbles.

The role played by helical disturbances in the dynamics of breakdown is a controversial issue. Two points of view have emerged: either breakdown itself results from the ultimate development of helical disturbances as primarily advanced by Ludwieg (1962) (for a critical discussion on the importance of asymmetries in breakdown, see Leibovich 1978, 1983), or breakdown is an independent phenomenon over which secondary helical disturbances may grow (a discussion in favour of this point of view may be found in Escudier 1988). The experimental observations are ambiguous: Lambourne (1965), Escudier & Zehnder (1982) and Brücker & Althaus (1995) report that the bubble is the basic form but that it becomes unstable to helical disturbances and changes into the spiral form. By contrast, Sarpkaya (1971) and Faler & Leibovich (1977) have observed that the bubble is a secondary development of the primary spiral form. Interestingly, one should note that a similar confusion also exists regarding the winding direction of the spiral as one proceeds downstream: the first group of authors states that the direction of rotation of the spiral is opposite to the primary vortex while the latter observe a corotation.

Vortex breakdown is also a temporally evolving phenomenon. Unsteady and asymmetric recirculating motions occur in the 'stagnant' region within the bubble. As described by Sarpkaya (1971) and Brücker & Althaus (1992), fluid is injected into and ejected out of the internal region by an emptying and filling process taking place in the downstream part of the bubble and involving a gyrating tilted vortex ring. The whole spiral is observed to precess as a solid body around the axis in the same direction as the upstream vortex (Lambourne & Bryer 1961; Faler & Leibovich 1977; Brücker 1993). Furthermore, according to Faler & Leibovich (1977), breakdown states display secondary temporal dynamics and wander back and forth along the axis in a random fashion.

The present investigation differs from previous experimental studies in several important respects. We adopt a swirling jet experimental set-up where confinement effects are negligible since the jet exhausts into a large water tank. Furthermore, the axial and azimuthal velocities of the basic flow can be monitored independently, swirl being imparted to the fluid by a motor that sets a honeycomb into rotational motion

https://doi.org/10.1017/S0022112098002870 Published online by Cambridge University Press

within a settling chamber. This set-up has led us to identify a new breakdown configuration in the form of a conical sheet, which is clearly distinct from the previously known nearly closed bubble state. In contrast with earlier qualitative investigations, the presence of hysteresis is characterized quantitatively by systematically varying the swirl parameter near threshold. An additional advantage of the present experimental apparatus lies in the fact that breakdown can easily be visualized in cross-sections perpendicular to the jet axis. Thereby, one can unambiguously determine whether the swirling jet is axisymmetric or not. We also could ascertain that the cone typically undergoes secondary temporal dynamics and that recirculating motions are present within the stagnant region.

Sarpkaya (1995) and Khoo *et al*. (1997) have also reported observing a conical vortex breakdown but we believe that the flow structure identified here and in Billant, Chomaz & Huerre (1994) and Billant, Chomaz & Delbende (1994) is qualitatively different from these authors' observations. The conical state reported by Sarpkaya (1995), which occurs for very high Reynolds numbers of order 10^6, is in fact a bubble whose turbulent conical wake has come so close to the stagnation point that the whole structure looks like a cone. A gradual change from the classical bubble to a turbulent conical bubble can be followed as Re is increased from 50 000 to 200 000. Similar remarks apply to the conical state reported by Khoo *et al*. (1997) which is observed only at higher Reynolds numbers than the bubble or the spiral ($3200 < Re < 3600$). It simply appears as the natural evolution of the wake of a bubble towards a turbulent state as Re is increased. The cone opening angle is about 20° in the case of Sarpkaya (1995) and 40° in the case of Khoo *et al*. (1997). These states display none of the characteristics of the laminar cone reported herein which, by contrast, is observed for the same parameter values as the bubble and has a characteristic opening angle of 90°.

A large number of numerical studies have been devoted to the simulation of vortex breakdown in swirling pipe flow: the steady and unsteady axisymmetric incompressible Navier–Stokes equations have been numerically integrated by Kopecky & Torrance (1973), Grabowski & Berger (1976) and Krause, Shi & Hartwich (1983). As extensively reviewed by Althaus *et al*. (1995), recent time-dependent three-dimensional simulations have reproduced not only the unsteadiness and asymmetry of the internal flow within the bubble (Spall, Gatski & Ash 1990) but also the spiral breakdown (Gatski & Spall 1991).

Vortex breakdown has been the subject of many somewhat conflicting theories. The main keywords characterizing the various theoretical approaches typically are: hydrodynamic instability, flow stagnation, conjugate states. For a comprehensive presentation, the reader is referred to the surveys of Hall (1972), Leibovich (1978, 1983), Stuart (1987), Escudier (1988), Delery (1990) and Althaus *et al*. (1995). In the spirit of the two-stage transition theory proposed by Escudier & Keller (1983), a simple criterion for the occurrence of cone breakdown will be presented in § 2.

Flows with conical similarity where the velocity field is inversely proportional to the distance from the origin are widely encountered in vortex dynamics (Goldshtik 1960; Long 1961; Shtern & Hussain 1993). In the context of the present investigation, it is interesting to note that Goldshtik (1960) has derived a family of exact self-similar conical solutions of the Navier–Stokes equations which exhibit interesting features such as non-uniqueness and hysteresis. A particular solution bearing some resemblance to the swirling jet configuration is the vortex filament with an axial velocity component considered by Goldshtik (1979) where two conical flow solutions may coexist in a certain parameter range.

https://doi.org/10.1017/S0022112098002870 Published online by Cambridge University Press

The present investigation is organized as follows. A simple theoretical criterion for breakdown is derived in § 2. The experimental set-up and procedure are presented in § 3. The various breakdown states and their domains of existence in control parameter space are documented in § 4. In § 4.1, the breakdown states are characterized by means of flow visualizations and LDA measurements. In § 4.2, the critical values for the onset of breakdown are presented in the Reynolds number–swirl parameter plane. The theoretical breakdown criterion of § 2 is compared with experiments in § 4.3. The spatial evolution of the local swirl parameter along the jet axis is investigated in § 4.4. In § 4.5, we discuss the determining factors governing the selection of the bubble or cone states. In § 5, we follow the typical sequence of events taking place as the swirl parameter is gradually increased from zero up to the occurrence of breakdown. The hysteresis phenomena associated with the breakdown transition are fully documented in § 6. The axisymmetric nature of the breakdown states or lack thereof is examined in § 7 and the secondary dynamics of the cone and the bubble configurations is described in § 8. Finally, the main results of the study are summarized in § 9.

2. Theoretical considerations: a simple vortex breakdown criterion

The aim of this section is to derive a necessary condition for the onset of vortex breakdown in a flow of infinite extent. The usual cylindrical coordinate system (x, r, θ) is used, where x denotes the axial distance, r the radial distance and θ the azimuthal angle. (V_x, V_r, V_θ) designate the velocities in the corresponding directions.

In analogy with hydraulic jumps, the conjugate flows analysis of Benjamin (1962) characterizes vortex breakdown as a dissipative axisymmetric jump-like transition between two distinct inviscid states: an upstream ('supercritical') state where only infinitesimal downstream travelling waves can exist and a downstream ('subcritical') state upon which standing waves can occur. Since Benjamin (1962) argued that the axial momentum flux in the downstream state must always be greater than its counterpart in the upstream state, the existence of a region of vigorous turbulence, supposed to coincide with vortex breakdown, was postulated to account for the difference in axial momentum flux. Benjamin (1962)'s conclusion that the transition is always dissipative is paradoxical since a smooth transition with no evidence of dissipation is observed in the experiments. In the first stage of their two-stage transition theory, Escudier & Keller (1983, 1985) and Keller, Egli & Exley (1985) managed to prove that this earlier conclusion of Benjamin (1962) is erroneous. By considering a generalized variational principle with an arbitrarily specified shape of the downstream vortex profile allowing for hollow-core flows, Escudier & Keller (1983) demonstrate that the difference in axial momentum flux between the two states can indeed vanish. As an example, these investigators discuss in detail the case of the Rankine vortex. By assuming uniform upstream and hollow downstream vortex states separated by a transition region, a criterion for breakdown is directly derived from the condition that the axial momentum flux be conserved. The main assumption is that the cavity of the downstream hollow vortex is at stagnation pressure with negligibly small velocity inside.

In what follows, we consider, as Escudier & Keller (1983), that breakdown is a non-dissipative axisymmetric transition between two distinct states and that velocities inside the stagnation zone are negligible. A criterion is obtained by simple considerations in the case of a free vortex undergoing conical breakdown in a flow of infinite extent. The basic idea, as shown by Hall (1966), is the following: if the radius of the vortex increases in x, the conservation of circulation implies an axial increase

https://doi.org/10.1017/S0022112098002870 Published online by Cambridge University Press

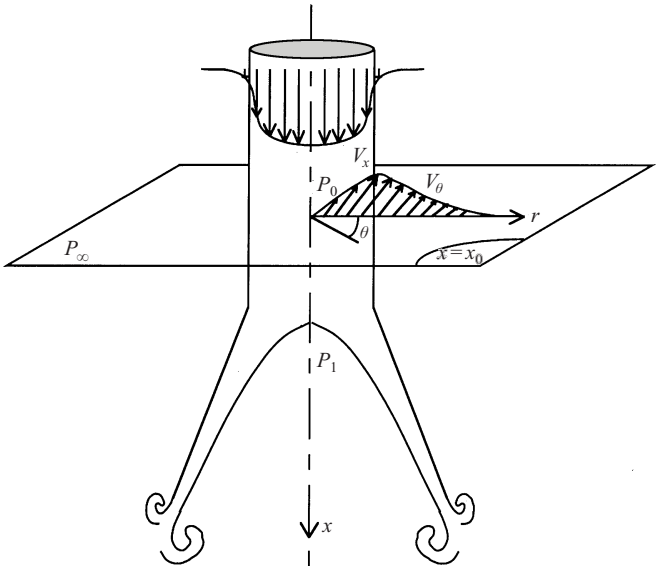


FIGURE 1. Schematic configuration of cone vortex breakdown.

in pressure in the vortex core which leads to an axial deceleration. When the axial increase in pressure is sufficient to bring the axial velocity to zero, a stagnation point appears and vortex breakdown may take place.

Consider a free vortex displaying a steady stagnation point on the axis and opening into a cone in the downstream direction (figure 1). According to the Bernoulli equation applied along the streamline on the axis of the vortex, the total head $H = P/\rho + \frac{1}{2}(V_x^2 + V_r^2 + V_\theta^2)$ reads

$$H = P_0/\rho + V_x^2(0, x_0)/2 = P_1/\rho\,, \tag{2.1}$$

where P_0 is the pressure on the vortex axis at station x_0 located well upstream of the stagnation point, ρ is the fluid density, $V_x(0, x_0)$ is the upstream axial velocity on the vortex axis at x_0 and P_1 the pressure at the stagnation point. Far upstream of the stagnation point, the radial pressure gradient is balanced by the centrifugal force, consequently

$$P_0 = P_\infty - \int_0^\infty \rho \frac{V_\theta^2(r, x_0)}{r} \mathrm{d}r\,, \tag{2.2}$$

where $V_\theta(r, x_0)$ is the azimuthal velocity and P_∞ the ambient pressure at infinity in the cross-stream plane $x = x_0$.

Following Escudier & Keller (1983), we assume that, to a good approximation, the velocities inside the stagnation zone vanish although some weak internal recirculating motion may exist resulting from instabilities and viscous contamination. The stagnation zone of the cone is open to the surrounding fluid which is at rest at infinity. Thus, the absence of steady motion between the quiescent surrounding fluid and the stagnation zone suggests that no steady pressure gradient exists and we shall assume the identity $P_1 = P_\infty$. This argument is the essential ingredient which distinguishes the present reasoning from the theory of Escudier & Keller (1983). In the latter, the pressure P_1 is deduced from the conservation of axial momentum. Note that pressure measurements carried out by Farokhi *et al*. (1988) in a free swirling jet fully support

https://doi.org/10.1017/S0022112098002870 Published online by Cambridge University Press

the assumption that the pressure in the stagnation zone is indeed equal to the pressure P_∞.

Thus, upon exploiting this identity and eliminating the pressures in (2.1) and (2.2), one obtains the simple relation

$$\frac{\displaystyle\int_0^\infty \frac{V_\theta^2(r,x_0)}{r}\mathrm{d}r}{V_x^2(0,x_0)} = \frac{1}{2}. \tag{2.3}$$

We emphasize that relation (2.3) is only a necessary condition: if, for any reason, a vortex experiences an expansion of its core in the form of an open cone, then the occurrence of a stagnation point necessarily requires that the above criterion be satisfied.

In the particular case of a Rankine vortex, i.e. solid body rotation $V_\theta = \Omega r$ and $V_x = \text{const.}$ for $r < a$ and irrotational flow $V_\theta = \Omega a^2/r$ and $V_x = 0$ for $r > a$, this criterion reduces to

$$\frac{V_{\theta\,max}(x_0)}{V_x(0,x_0)} = \frac{1}{\sqrt{2}}, \tag{2.4}$$

where $V_{\theta\,max}(x_0) = \Omega a$ is the maximum azimuthal velocity. Please note that equation (2.3) holds for any velocity profile whereas (2.4) is a consequence of (2.3) which is only valid for a Rankine vortex. We recover the critical value obtained by Escudier & Keller (1983) for a Rankine vortex in the limit where the ratio of the vortex core radius to the tube radius vanishes, i.e. when confinement is negligible.

In the case of a bubble state, the stagnant region is not directly connected to the surrounding outer quiescent fluid. The relation $P_1 = P_\infty$ has therefore to be replaced by the weaker inequality $P_1 \leqslant P_\infty$. In all other respects, the previous reasoning holds and criterion (2.3) becomes

$$\frac{\displaystyle\int_0^\infty \frac{V_\theta^2(r,x_0)}{r}\mathrm{d}r}{V_x^2(0,x_0)} \geqslant \frac{1}{2}, \tag{2.5}$$

the value $1/2$ now being a lower bound for the bubble state to appear.

These criteria are compared with experiments in § 4.3.

3. Experimental set-up and procedure

3.1. *Experimental apparatus*

The experimental set-up, sketched in figure 2, consists of a vertical swirling jet discharging into a large water tank (Wu *et al.* 1992).

The jet axial velocity is generated by the hydrostatic pressure difference between two constant-head reservoirs. An overflow tank and a pump close the water circuit. The flow rate is controlled by a valve and flowmeter located on the exit pipe at the bottom of the tank. A filter located on the exit pipe of the pump cleans the water of any impurities. The homogeneity of water temperature in the whole circuit was carefully checked and monitored: maximum temperature differences were kept below 0.1 °C–0.2 °C.

A swirl velocity component is imparted to the jet by means of a motor and two concentric cylinders in the following way (see figure 3): the outer cylinder is fixed and the inner cylinder, which is 40 cm long and 18.5 cm in diameter, is set into rotational motion by a motor, and connected to the outer cylinder by a bearing track.

https://doi.org/10.1017/S0022112098002870 Published online by Cambridge University Press

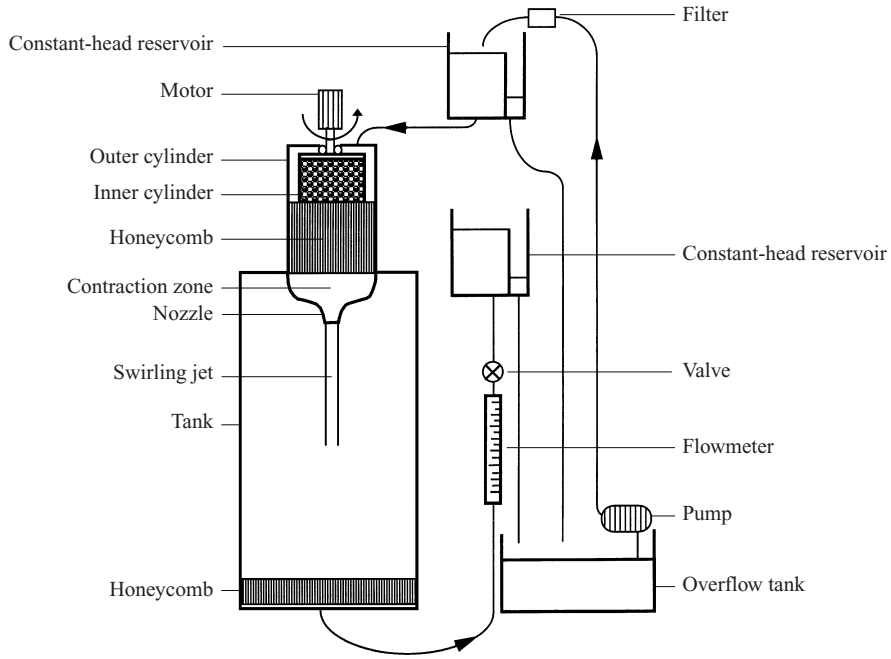


FIGURE 2. Sketch of experimental apparatus.

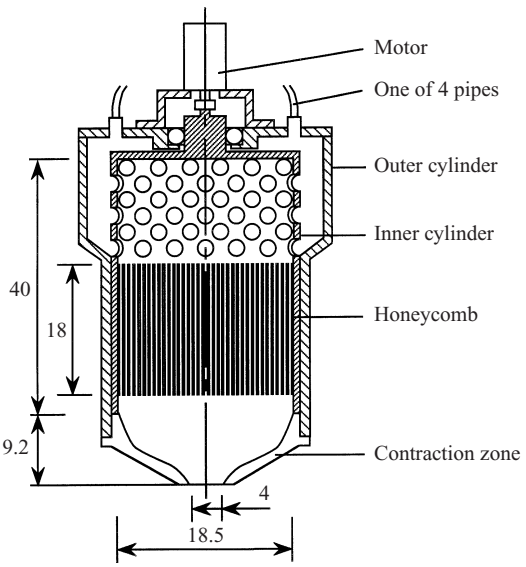


FIGURE 3. Detailed configuration of rotating system and nozzle. Dimensions are in cm.

The rotation rate of the motor is maintained constant by means of a servo control. The liquid is supplied from the upper constant-head reservoir to the outer cylinder through four pipes symmetrically placed on its top surface. Water is then fed to the inner cylinder through a network of holes regularly drilled on its upstream part. The flow is set into a state of solid body rotation and kept laminar by inserting an 18 cm long honeycomb into the inner rotating cylinder. The swirling jet ends in a smooth

https://doi.org/10.1017/S0022112098002870 Published online by Cambridge University Press

converging nozzle attached to the outer cylinder and mounted on top of a large transparent tank of square cross-section $120\times40\times40$ cm^3 (figure 2). The contraction zone is designed according to the optimum method (Mikhail 1979) in order to avoid flow separation. The exit diameter of the contraction zone is $D_1 = 40$ mm. But for comparison purposes, we have also used a nozzle of exit diameter $D_2 = 25$ mm that is inserted into the former. It should be emphasized that the relative large size of the test tank minimizes the effect of confinement and measured recirculation currents were found to be negligible. To further ensure quiescent flow conditions, a honeycomb is placed at the bottom of the tank, upstream of the exit pipe (figure 2), in order to avoid any whirlpool occurring.

Regular tap water is used but it is stocked in the same room several days ahead of time in order to eliminate air bubbles and to reach ambient temperature.

3.2. *Visualization and quantitative measurement techniques*

The flow is visualized by the laser induced fluorescence technique. Fluorescein dye is introduced in each of the four exit pipes of the upper constant-head reservoir (figure 2). Owing to different Lagrangian times within the rotating system, the dye is not always homogeneously radially distributed within the jet when the dye injection is started or stopped. But the dye concentration is always azimuthally homogeneous and steady. The light source consists of a 1 W Argon laser. The light sheet produced by a cylindrical lens is shone either in a meridional plane through the jet axis or in a horizontal plane perpendicular to the axis of rotation. In the latter case, the camera views the light sheet from below at an angle of about 45°, resulting in a parallax effect that may be corrected by image processing when needed. Images are recorded with a black and white 740×480 pixels CCD camera and captured by a video recorder or directly on a Macintosh. Various procedures such as the determination of the stagnation point location are carried out on the images by making use of the public domain NIH Image processing software (developed at the US National Institute of Health and available on the Internet at http://rsb.info.nih.gov/nih-image/) on a Macintosh.

In order to gain a three-dimensional understanding of the jet structure for some of the observed flow states, two laser sheets are simultaneously produced in a meridional plane and in a slanted plane at about a 20° angle from the horizontal. The first sheet produced by a 5 W Argon laser is obtained by reflection of the laser beam on a vibrating mirror and the second sheet is the same as previously described. The camera is then located along a direction perpendicular to the meridional plane.

Axial and azimuthal velocities are measured by two–component optical fibre laser Doppler anemometry (Dantec enhanced Burst Spectrum Analyser powered by the 5 W Argon laser) in backscatter mode. The probe volume, based upon a 400 mm focal length and a beam separation of 38 mm, is 0.19 mm in diameter and 5.3 mm in length but the effective length is considerably lower. Water is seeded with titanium oxide or ioridin particles. The laser probe is mounted on traversing mechanisms which allow accurate displacements in the axial and radial directions. The burst signals are fed through two burst spectrum analysers (BSA). Data transfers, control of the BSA as well as control of the traversing mechanisms and motor are performed by a Macintosh via an IEEE 488 interface. Vortex velocity profiles are measured in 2 mm steps. For a measurement at one location, data are acquired until either 1000 bursts have been collected or acquisition has lasted one minute. For typical data rates, most measurements consist of the mean of 1000 bursts. It typically takes 30 minutes to complete a traverse in the radial direction.

https://doi.org/10.1017/S0022112098002870 Published online by Cambridge University Press

3.3. *Experimental procedure and control parameters*

In order to explore parameter space, experiments have been conducted by varying the rotation rate while maintaining the flow rate constant. The rotation rate of the motor is slowly increased from zero in steps of approximately 17% of the final rotation rate needed for breakdown. Fine step-like increases are made possible by the servo control of the motor which allows accurate and minute variations of the rate of rotation. A stationary hydrodynamic regime is reached by waiting for at least 15 mn at each step. Close to the breakdown threshold, the rotation is increased extremely slowly in steps between 2.5% and 5% with a 15 mn waiting time between each step-like increase. The onset of breakdown is detected by flow visualizations. Further increases of the rotation rate can be produced in order to study the dynamic response of the breakdown state. A similar procedure is followed when the rotation rate is decreased.

The two independent 'degrees of freedom' of the experimental apparatus, namely the flow rate and the rotation rate, can be expressed in terms of two non-dimensional parameters: the Reynolds number and the swirl parameter. In order to define quantities which optimally describe the flow regime, we have chosen to introduce non-dimensional parameters based on the velocities directly measured in the swirling jet close to the nozzle exit plane and not on the imposed external parameters.

The swirl parameter, which is a measure of the ratio of azimuthal to axial velocities, is defined as follows:

$$S \equiv \frac{2V_\theta(R/2, x_0)}{V_x(0, x_0)}, \tag{3.1}$$

where x_0 is the shortest axial distance measured from the nozzle exit plane at which the measurement of both components is possible due to optical constraints: $x_0 = 5$ mm for the D_2 nozzle and $x_0 = 24$ mm for the D_1 nozzle. The azimuthal velocity $V_\theta(R/2, x_0)$ is measured at half the radius of the nozzle exit $r = R/2$; The axial velocity $V_x(0, x_0)$ is measured on the axis of the jet. The quantity $\Omega = 2V_\theta(R/2, x_0)/R$ characterizes the angular velocity of the vortex core, but note that it is not strictly speaking the slope of V_θ at $r = 0$ as in some other definitions of the swirl parameter. The convenient definition (3.1) is effectively obtained by measuring velocities at only two locations. Furthermore, from the various azimuthal velocity profiles displayed in figure 4(*a*), also note that $V_\theta(R/2, x_0) \approx V_{\theta\,max}(x_0)$ which will allow comparison of the critical values of (3.1) with the criterion (2.4). Another definition of the swirl parameter based on axial fluxes of azimuthal and axial momentum is commonly used in the literature on swirling jet flows (see, for instance, Farokhi *et al*. 1988; Panda & McLaughlin 1994). However, Farokhi *et al*. (1988) have shown that this definition is inappropriate for studying vortex breakdown: two swirling jets with completely different exit velocity profiles may then have the same value of the swirl parameter although only one experiences breakdown.

The Reynolds number is defined as

$$Re \equiv \frac{2R\bar{V}_x(x_0)}{\nu}, \tag{3.2}$$

where $\bar{V}_x(x_0)$ is the mean axial velocity in the jet and ν is the kinematic viscosity of water. In practice, the mean axial velocity in the jet is taken to be $\bar{V}_x(x_0) = V_x^{S=0}(0, x_0)$ because the axial velocity in the absence of rotation ($S = 0$) displays an almost flat top-hat profile (figure 4*b*). Under this condition, the axial velocity at $r = 0$ provides a good estimate of the mean axial velocity in the jet.

Figure 4 illustrates the velocity profiles measured at $x = x_0$ when S is varied

https://doi.org/10.1017/S0022112098002870 Published online by Cambridge University Press

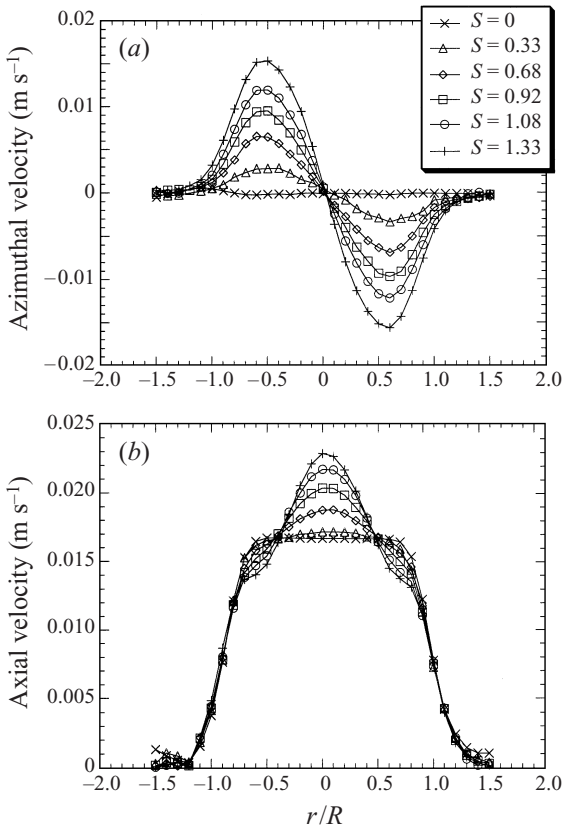


FIGURE 4. (*a*) Axial and (*b*) azimuthal velocity profiles at $x_0 = 24$ mm for various swirl parameters S; $Re = 666$, D_1. Increasing rotation distorts the axial velocity profile near the axis from its flat shape at $S = 0$. Note that the azimuthal velocity is approximately maximum at $r \approx R/2$.

and Re remains fixed. When $S = 0$, the axial velocity profile is top-hat. But as S is gradually increased, the azimuthal and axial components of the motion interact in a non-trivial manner due to the presence of the contraction which results in the distortion of the axial velocity profile near the axis (figure 4*b*). This effect is due to the increase of angular velocity through the contraction zone which leads to a decrease of the pressure near the axis. The induced axial pressure gradient implies an axial acceleration of the flow on the vortex axis. This increase in axial velocity is not linear with angular velocity so that the variations of swirl parameter with the rotation rate of the motor display a saturation trend.

Conversely, when the rotation rate of the motor is kept constant, the angular velocity Ω increases with Re (figure 5). This behaviour is also encountered in confined tubes (Leibovich 1978; Althaus *et al*. 1995) and generally explained by a decrease in vortex-core size of the type $DRe^{-1/2}$. However, in our situation, the vortex core radius remains nearly constant as seen from figure 5(*a*). The increase of circulation with flow rate is probably a complex effect of our rotating system.

Since the swirl parameter (3.1) is measured directly in the upstream flow at each incrementation of the motor rotation rate, a difficulty of interpretation arises when the swirling jet experiences breakdown close to the nozzle: the swirl parameter can then only be measured a short distance upstream of the stagnation point.

https://doi.org/10.1017/S0022112098002870 Published online by Cambridge University Press

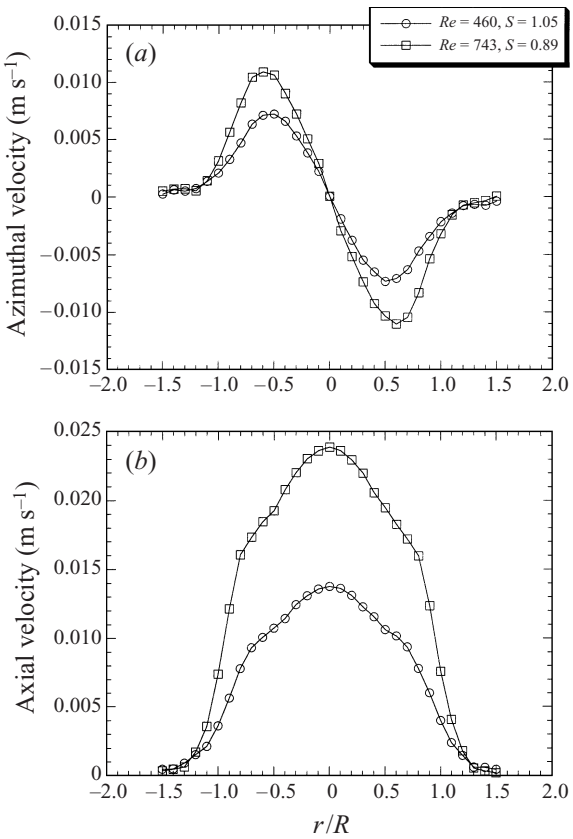


FIGURE 5. (*a*) Axial and (*b*) azimuthal velocity profiles at $x_0 = 24$ mm for the same rotation rate of the motor $\omega = 0.44$ r.p.m., but for two different Reynolds numbers $Re = 743$ and $Re = 460$; D_1. A higher axial velocity produces a stronger azimuthal velocity. The vortex-core size defined by the radius where V_θ is maximum is similar for $Re = 743$ and for $Re = 460$.

Consequently the measurement is affected by the presence of the stagnation point and it is not an objective estimate of the swirl parameter imposed 'far upstream'. In order to circumvent this difficulty, the breakdown thresholds Sc_a and Sc_d for onset and disappearance of breakdown respectively (see § 4.2) are based upon the values measured at the step preceding breakdown onset and at the step just after its disappearance. This procedure is sufficiently accurate since the rotation rate is varied in small steps of 2.5–5% of the final rotation rate needed for breakdown onset. Because of the saturation trend of the swirl parameter variations with rotation rate of the motor, this protocol introduces at most a relative error of only 1% on the actual value of Sc.

However, when the true swirl value is needed and breakdown has actually taken place, the swirl parameter is extrapolated from the data measured at the steps preceding breakdown through a least square fit with the function $S = a(1 - \exp(b\omega))$, where ω is the angular velocity of the motor and (a, b) are fitting constants computed for each experiment. Such an extrapolation is only performed to yield the corresponding value of the swirl parameter in figure captions and to study the variations in the location of the stagnation point with swirl parameter.

https://doi.org/10.1017/S0022112098002870 Published online by Cambridge University Press

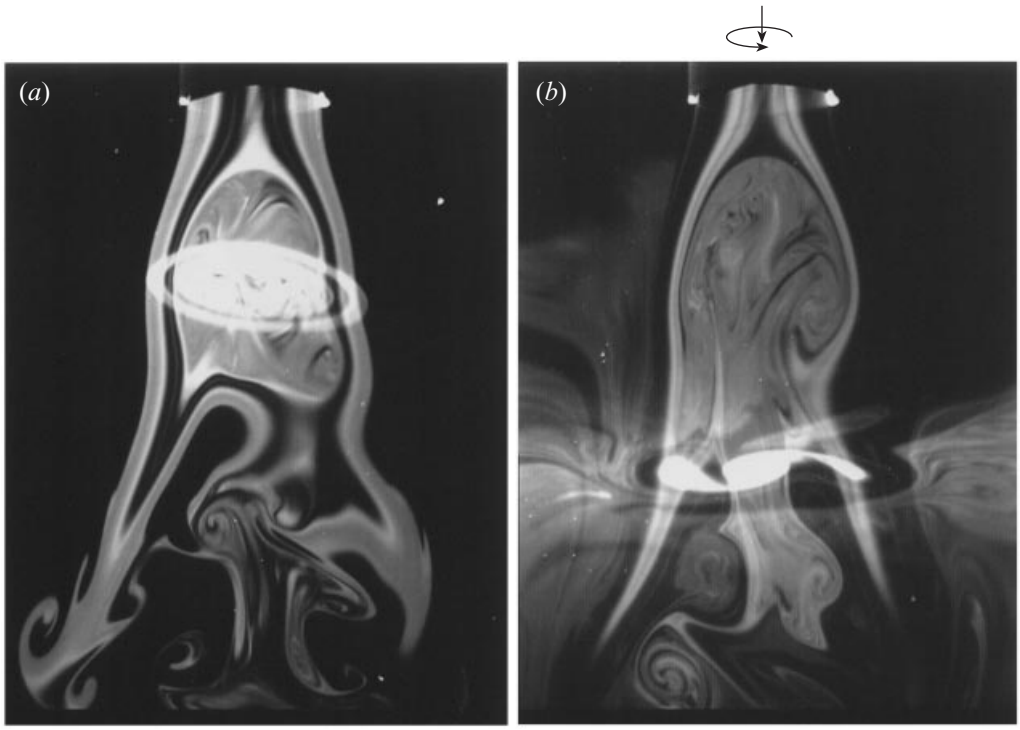


FIGURE 6. Flow visualizations of bubble for $Re = 606$, $S = 1.42$, D_2. Two laser sheets are simultaneously produced in a meridional plane and in a slanted plane from the horizontal. The upstream portion (*a*) is axisymmetric unlike the tail (*b*) of the bubble. Note that for the visualizations where both lasers were used simultaneously, the parameters *Re* and *S* could not be measured by LDA and were deduced by extrapolation, but with less precision, from the imposed global parameters: flow rate and rotation rate.

4. Portrait of the various breakdown states

For ease of presentation, we first discuss the observed flow states from a static point of view: the various breakdown configurations observed and the flow regime diagrams are the main focus of the present section. A more dynamical point of view, i.e. the evolution of the flow structures as a function of S is taken in § 5.

4.1. *An attempt at classifying vortex breakdown states*

Four distinct breakdown states have been identified: two main configurations, the bubble and the cone, and two related configurations, the asymmetric bubble and the asymmetric cone. A common feature of these states is the presence of a stagnation point which is located on the axis for the bubble and the cone, or which undergoes precession around the axis in the case of the asymmetric bubble and the asymmetric cone. The characteristics of the flow downstream of the stagnation point markedly differ for the bubble and the cone.

Since the bubble has already been extensively documented in confined tubes experiments (Sarpkaya 1971; Faler & Leibovich 1977), our discussion will be kept as brief as possible. Figure 6 illustrates typical flow visualizations of a bubble. Two laser sheets were produced in a meridional plane through the jet axis and in a slanted plane at a 20° angle from the horizontal, the latter cutting through the middle of the bubble in figure 6(*a*) and through its tail in figure 6(*b*). Fluorescein dye is not

https://doi.org/10.1017/S0022112098002870 Published online by Cambridge University Press

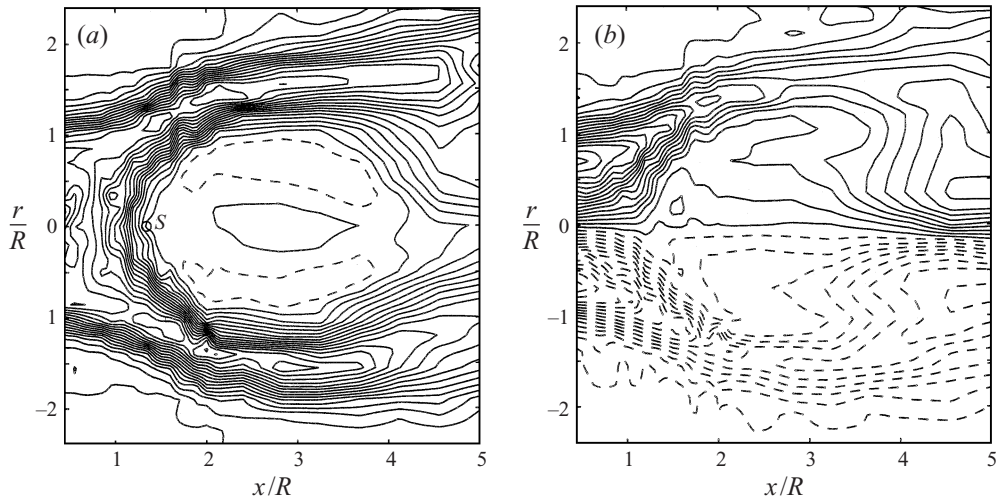


FIGURE 7. Contours of constant axial (*a*) and azimuthal (*b*) velocity measured by LDA in a bubble for $Re = 687$, $S = 1.4$, D_2. Contour interval is 0.155 cm s^{-1}. Negative contours are indicated by dashed lines. The location of the front stagnation point is indicated by a circle.

uniformly distributed in the jet because the injection was either beginning (figure 6*a*) or ending (figure 6*b*). The vortex expands abruptly at a streamwise station located $0.5D$ from the nozzle exit and encloses an ovoid region of slow recirculating flow. The bubble size is $1.5D - 2.5D$ in diameter as well as in streamwise extent. The upstream inner surface has a paraboloid shape. The comparison between figures 6(*a*) and 6(*b*) indicates that the upstream region of the bubble is axisymmetric unlike the downstream portion where a spiral with two arms is seen. The entire upstream configuration of the bubble, i.e. the axial location of the stagnation point and the bubble diameter, is almost stationary. The tail is not steady and farther downstream, the flow is disordered. In order to complement the visualizations by quantitative measurements, axial and azimuthal velocity contours measured by LDA are displayed on figure 7(*a*,*b*). Azimuthal and axial velocities are very weak in the internal zone compared with those in the surrounding flow. The axial velocity contours (figure 7*a*) indicate that the internal zone is filled in its outer periphery and emptied in the region around the axis, a feature consistent with the two-celled internal structure revealed by the LDA measurements in confined tubes of Faler & Leibovich (1978). The axial velocity contours resemble the instantaneous contours obtained by Spall *et al*. (1990) in unsteady three-dimensional numerical simulations. Typical fluctuation levels around the averaged velocities are of the order of 0.4 cm s^{-1} in the downstream part of the bubble and 0.1 cm s^{-1} in its upstream part in the stagnation zone. The level of axisymmetry and the nature of the recirculating flow are examined in § 7 and § 8 respectively.

The cone, which seems not to have been observed previously, is shown on figure 8†. As in figure 6, two laser sheets were also used. In sharp contrast with the bubble, the expansion of the vortex at the stagnation point is not followed farther downstream by a contraction, i.e. a flow toward the axis enclosing a stagnation zone. This breakdown state takes the form of a conical sheet flowing over an open

† A colour image can be viewed and/or downloaded on the Internet at http://www.ladhyx.polytechnique.fr/

https://doi.org/10.1017/S0022112098002870 Published online by Cambridge University Press

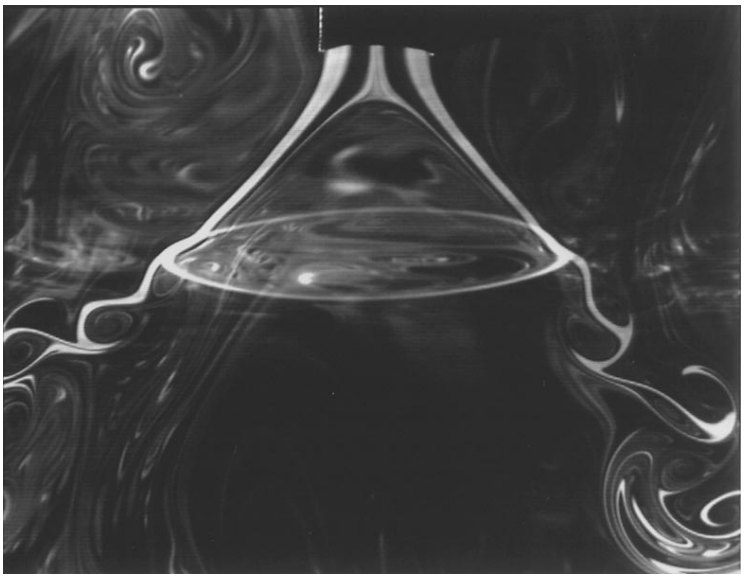


FIGURE 8. Flow visualization of cone for $Re = 606$, $S = 1.37$, D_2. Two laser sheets are simultaneously produced in a meridional plane and in a slanted plane from the horizontal. The cone is axisymmetric even far downstream. See remark in caption of figure 6 regarding the evaluation of Re and S.

region of stagnant fluid. As for the bubble, the inner surface near the apex has a paraboloid shape, but farther downstream it takes a conical shape. The thickness of the conical sheet continuously decreases with downstream distance from the stagnation point. Instabilities are observed to grow on the sheet so that, at about 2–3 diameters downstream of the stagnation point, the conical sheet distorts, rolls up into vortices before breaking into weak turbulence. These instabilities may result from the streamwise shear within the sheet or from a centrifugal instability due to the azimuthal motion within the sheet, or more probably from a combination of both. The flow within the cone is only quasi-steady: secondary recirculating currents are present but they are much weaker and slower than in the case of the bubble. We shall see in § 8 that the cone angle varies with time in a regular and well-defined fashion while the stagnation point wanders back and forth along the jet axis. Because of the slow secondary motion experienced by the cone, we have not been able to carry out reliable LDA measurements.

The asymmetric cone (figure 9) and the asymmetric bubble (figure 10) evolve from the cone and the bubble respectively and are observed for larger Re. They are qualitatively similar, except that a precessing motion of the stagnation point is superimposed on the dynamics. In the visualizations of figures 9 and 10, only one meridional laser sheet is shone through the flow. The precession is made evident by the fact that the stagnation point is not located on the nozzle axis but is slightly off axis. In figure 9, this eccentricity is further made visible by the deflection of a dyeless central filament as it approaches the stagnation point. The deformation of this particular filament is observed to wander regularly from one side of the jet axis to the other. The downstream extent of the conical sheet is about $1D$–$1.5D$, which is somewhat smaller than for the cone (figure 8). Indeed, since Re is larger, instabilities are likely to be stronger and the disorganization of the conical sheet moves upstream, closer to the stagnation point.

https://doi.org/10.1017/S0022112098002870 Published online by Cambridge University Press

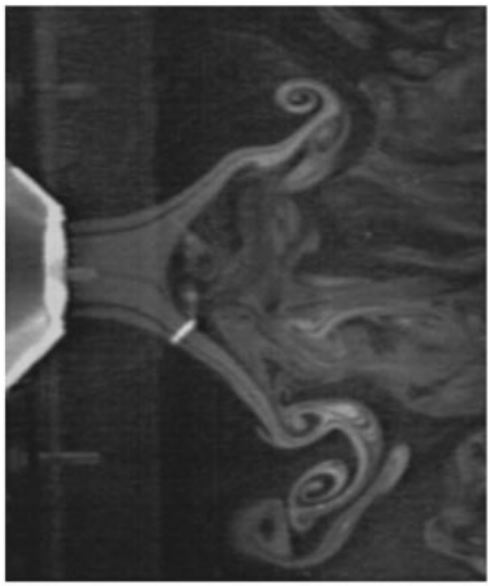


FIGURE 9. Flow visualization of asymmetric cone for $Re = 916$, $S = 1.31$, D_1. The eccentricity of the stagnation point is made visible in this photograph by the deviation of a lightly coloured central filament.

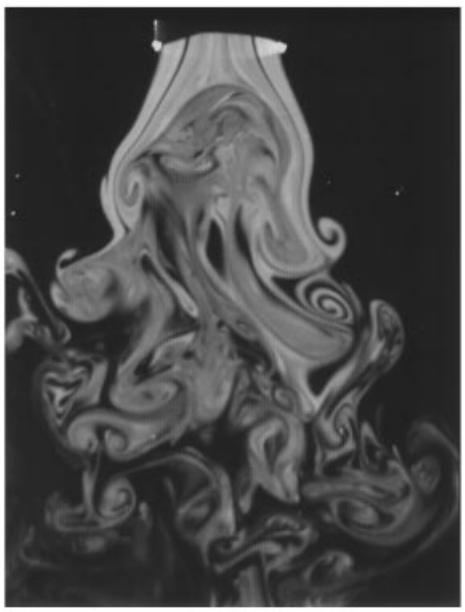


FIGURE 10. Flow visualization of asymmetric bubble for $Re = 1022$, $S = 1.35$, D_2. The stagnation point is located away from the axis and is observed to wander regularly from one side to the other.

The asymmetric bubble visualization (figure 10) also demonstrates the asymmetric nature of the flow in the stagnation point region to be compared with the perfect symmetry prevailing in the bubble case (figure 6). Instantaneous measurements of the two-dimensional velocity field pertaining to spiral breakdown made by Brücker

https://doi.org/10.1017/S0022112098002870 Published online by Cambridge University Press

(1993) exhibit a similar asymmetry. The eccentricity of the stagnation point was also observed to move with time from one side to the other. According to visualizations, recirculating motions within the stagnation zone are more intense and the downstream part of the asymmetric bubble is more open and unsteady than for the bubble. However, the asymmetric bubble is observed to undergo a noticeable contraction further downstream, a feature which clearly distinguishes it from the asymmetric cone state. Visualizations in a horizontal plane at axial locations close to the stagnation point have confirmed the precession of the asymmetric cone and asymmetric bubble in the same direction as the upstream vortex flow in agreement with Brücker (1993). The period of rotation is, for instance, 7 s for an asymmetric cone observed at $Re = 866$ with the D_1 nozzle and 4 s for an asymmetric bubble obtained with the D_2 nozzle at $Re = 1086$.

The instantaneous measurements of Brücker (1993) in a spiral type breakdown have revealed a strong similarity with the bubble: the spiral is nothing but a bubble with an off-axis stagnation point that rotates around the vortex axis. Therefore, when a single dye filament initially located on the jet axis is used for visualization, its deflection by the off-axis rotating stagnation point results in the formation of a characteristic spiral structure. The existence of a stagnation point in the vicinity of the first kink of the spiral is then inferred by the presence of dye tongues that move upstream towards the stagnation point (see photographs of spiral breakdown by Lambourne & Bryer 1961). The latter point is crucial in order to establish the existence of a spiral breakdown with a stagnation point because the flows under consideration are highly prone to helical instabilities that could also result in a spiral filament structure without requiring the presence of a stagnation point. We therefore expect that if a single filament of dye were used, the present asymmetric bubble would appear as a spiral breakdown. However, our observations differ in several respects from some previous studies in confined tubes (Sarkpaya 1971; Faler & Leibovich 1977; Garg & Leibovich 1979). For instance, we have observed that the asymmetric bubble lives in the same range of axial stations as the bubble. This is in sharp contrast with the aforementioned authors who report that the spiral state forms at axial locations well downstream of those for the bubble. Furthermore, these investigators report that, as the Reynolds number is increased, the spiral evolves into a bubble. In the present study, the opposite scenario holds: the bubble turns into an asymmetric bubble with increasing Reynolds number in agreement with the experiments of Brücker & Althaus (1995) and Althaus *et al*. (1995). Differences in the geometry of the various experiments might explain these discrepancies.

4.2. *Flow conditions in parameter space*

The experimental conditions that have been examined in detail are summarized in parameter space for each nozzle on figure 11(*a*,*b*). The symbols Sc_a and Sc_d denote the threshold values for appearance and disappearance of breakdown as the swirl is increased and decreased respectively. We recall that an objective measure of the swirl parameter could not be obtained in the presence of breakdown (see § 3.3). As a result, since the rotation rate is increased in small steps, Sc_a is based upon the value measured at the step immediately preceding breakdown. Conversely, Sc_d is the value measured at the step just beyond the disappearance of breakdown. Consequently, breakdown occurs when $S > Sc_a$ and, if there is no hysteresis, $Sc_a = Sc_d$. In the range of Reynolds numbers tested ($300 < Re < 1200$), vortex breakdown occurs when $S > 1.22$–1.42 for the D_1 nozzle (figure 11*a*) and $S > 1.28$–1.57 for the D_2 nozzle (figure 11*b*). The transition value shows no obvious trend with Reynolds number.

https://doi.org/10.1017/S0022112098002870 Published online by Cambridge University Press

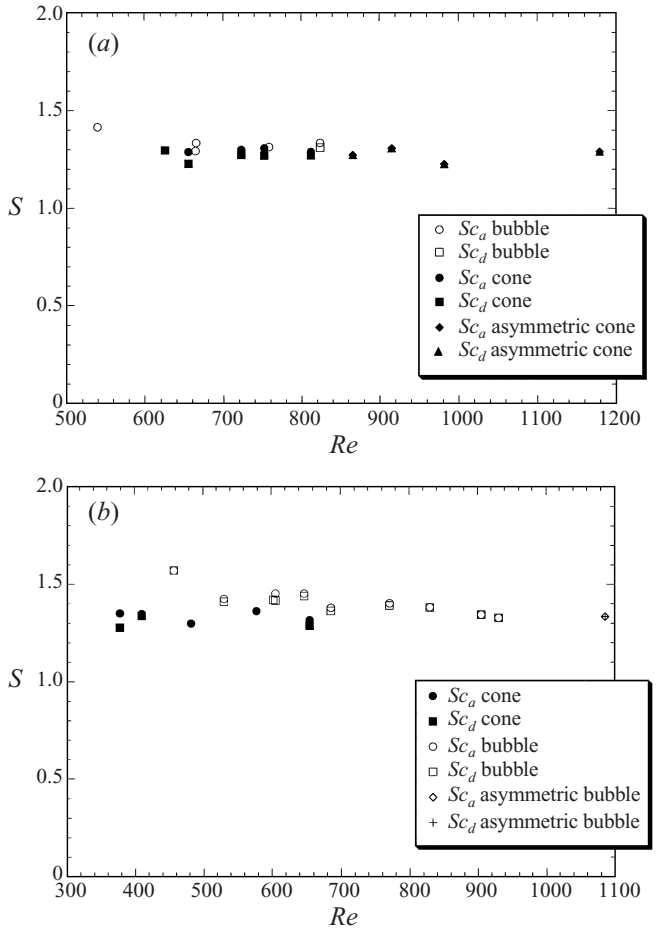


FIGURE 11. Critical values for appearance Sc_a and disappearance Sc_d of breakdown in (Re, S) parameter space for each nozzle: (*a*) D_1, (*b*) D_2.

Hysteresis has been observed in well defined domains. The upper limit in Reynolds number above which hysteresis is no longer detectable is similar for both nozzles: $Re = 839 \pm 27$ for D_1, and $Re = 918 \pm 13$ for D_2. Hysteresis is not observed when $Re \leqslant 626$ for D_1. Above Sc, the two main configurations, namely the bubble and the cone, have remarkably been observed for the same values of Reynolds number and swirl parameter. This apparent bistability is further discussed in § 4.5. The asymmetric bubble and cone are observed at larger Reynolds numbers than the bubble and the cone: the boundary between the axisymmetric and asymmetric states is located at $Re = 839 \pm 27$ for the D_1 nozzle and $Re = 976 \pm 45$ for the D_2 nozzle.

4.3. *Experimental validation of vortex breakdown transition criteria*

Several definitions of the swirl parameter have been introduced in the past in accordance with either the particular vortex model selected or the type of measurement used. Each definition is associated with a distinct breakdown criterion. Let us compare our experimental threshold with some of these criteria beginning with the one derived in § 2.

From the simple breakdown criterion (2.4) established in § 2 for the Rankine

https://doi.org/10.1017/S0022112098002870 Published online by Cambridge University Press

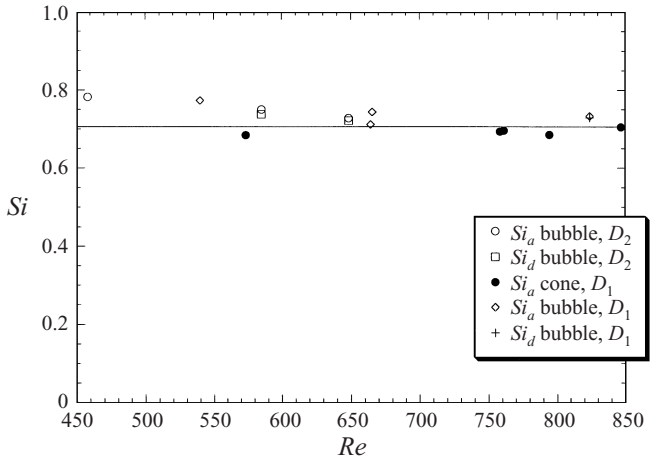


FIGURE 12. Critical values for appearance Si_a and disappearance Si_d of breakdown in (Re, Si) parameter space. The continuous line refers to the theoretical breakdown criterion (2.3) $Si = 1/\sqrt{2}$ established in § 2.

vortex, it is first possible to account for the measured critical value $Sc = 1.4 \pm 0.18$. As mentioned in § 3.3, the azimuthal velocity at $r = R/2$ is approximately equal to the maximum aximuthal velocity $V_\theta(R/2) \approx V_{\theta\,max}$. Consequently, according to equation (2.4), the theoretical value for the breakdown of a Rankine vortex is $Sc \approx 2V_{\theta\,max}/V_x(0, x_0) = \sqrt{2} = 1.41$ which is remarkably close to the experimental value $Sc = 1.4 \pm 0.18$.

For a more precise evaluation based on equation (2.3), the critical value of the interpolated parameter

$$Si = \frac{\left(\int_0^\infty \frac{V_\theta^2(r, x_0)}{r} \mathrm{d}r\right)^{1/2}}{V_x(0, x_0)}, \tag{4.1}$$

has been directly calculated from the actual velocity profiles measured at critical. Such data are available only for some experimental runs because most of the time, S and Re are obtained from single-location measurements and the detailed velocity profiles have not been measured. The experimental results are compared with the theoretical value $1/\sqrt{2} = 0.707$ predicted by criterion (2.3) on figure 12. Regardless of the breakdown type, bubble or cone, there is a reasonably good agreement with experimental observations, the discrepancy becoming larger at smaller Reynolds number. This criterion has also been tested on the two completely different velocity profiles measured in the swirling jet experiment of Farokhi *et al*. (1988). Criterion (2.3) applied to the profiles measured close to the nozzle exit correctly predicts the observations of these authors: $Si \approx 0.83 > 0.707$ for the swirling jet with breakdown while $Si \approx 0.58 < 0.707$ for the swirling jet without breakdown. This further confirms the validity of the breakdown criterion (2.3) which does not involve the nozzle diameter. It may therefore be concluded that the simple criterion (2.3) is capable of predicting quite accurately the onset of vortex breakdown. Note, however, that its derivation assumes no confinement and the outer pressure to be uniform. The presence of an outer adverse pressure gradient is widely known to be a critical factor in triggering vortex breakdown in confined tubes (Sarpkaya 1974; Escudier &

https://doi.org/10.1017/S0022112098002870 Published online by Cambridge University Press

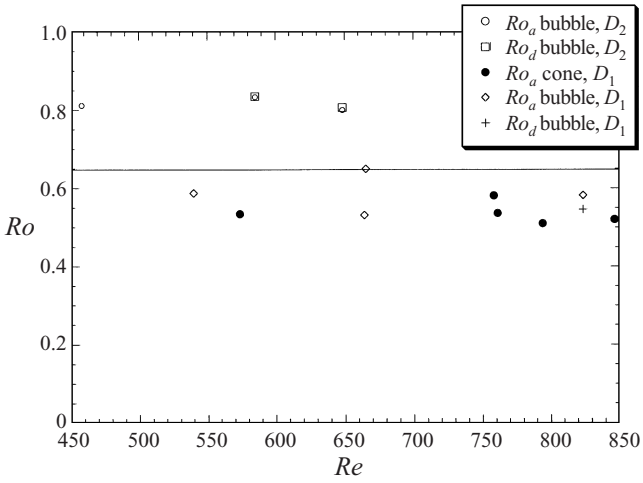


FIGURE 13. Critical values for appearance Ro_a and disappearance Ro_d of breakdown in (Re, Ro) parameter space for the same data as in figure 12. The continuous line refers to the empirical criterion $Ro_c = 0.65$ proposed by Spall *et al*. (1987).

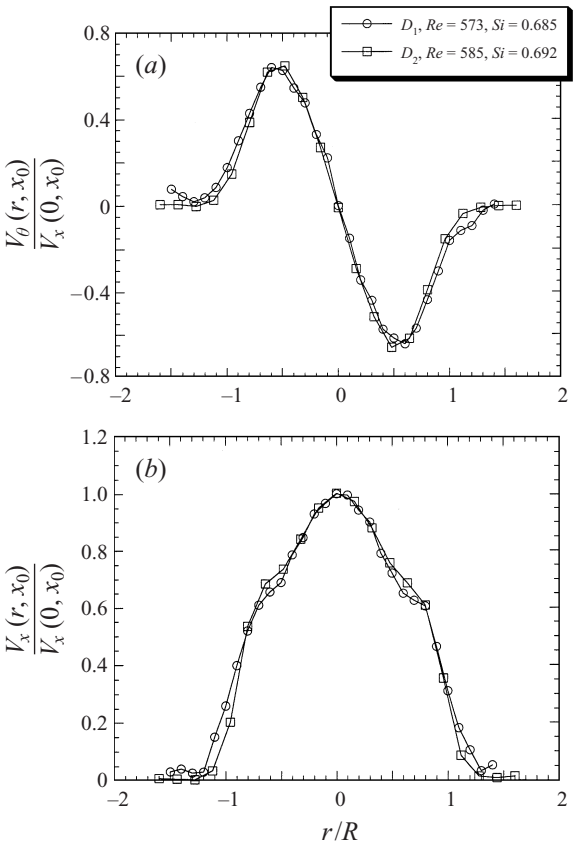


FIGURE 14. Comparison between the normalized (*a*) azimuthal $V_\theta(r, x_0)/V_x(0, x_0)$ and (*b*) axial $V_x(r, x_0)/V_x(0, x_0)$ velocity profiles of each nozzle at nearly the same parameters (Re, Si). A cone is observed for the D_1 nozzle. Subsequent increases in rotation rate lead to the formation of a bubble at $Si = 0.75$ for the D_2 nozzle.

https://doi.org/10.1017/S0022112098002870 Published online by Cambridge University Press

Zehnder 1982; Althaus *et al*. 1995). In such instances, the criterion derived here is not expected to apply.

Spall, Gatski & Grosh (1987) have proposed a breakdown criterion based on the Rossby number Ro (inverse of the swirl parameters) more precisely defined as $Ro = V_x(r^*, x_0)/r^*\Omega$, where $\Omega = \lim_{r\to 0} V_\theta(r, x_0)/r$ is the core angular velocity and r^* the radius of maximum azimuthal velocity. A survey of various experimental studies has led these authors to suggest the empirically determined critical value $Ro_c \approx 0.65$. The experimental critical Rossby number Ro_c is displayed in figure 13 for the same experimental data as in figure 12. The results of the various experimental runs are somewhat dispersed and a definite dependence on nozzle diameter is noticeable: $Ro_c = 0.51$–0.65 for the D_1 nozzle and $Ro_c = 0.80$–0.84 for the D_2 nozzle. The reason for this dependence on nozzle diameter lies in slight differences in the velocity profiles around the radius r^* of maximum azimuthal velocity: as shown on figure 14, normalized azimuthal velocity profiles are nearly identical for both nozzles while normalized axial velocity profiles noticeably differ in the range $0.5 < r/R < 1$, for almost the same values of the control parameters Re and Si.

Other investigators (see, for instance Sarpkaya 1971) use as critical control parameter for the onset of breakdown, the maximum swirl angle Sa defined as the arctangent of the ratio between azimuthal and axial velocity. For the same experimental data as in figure 12, the critical maximum swirl angle Sa is found to be in the range $44.5°$–$49°$ for the D_1 nozzle, and in the range $43.3°$–$43.6°$ for the D_2 nozzle. By comparison, Sarpkaya (1971) reports a critical value of about $50°$ for the bubble, regardless of Reynolds number.

4.4. *Axial evolution of swirl parameter*

The axial variations of the swirl parameter $S(x)$ have been documented when the swirl parameter $S = S(x_0)$ is slightly above the threshold of breakdown. The local swirl parameter $S(x)$ defined as in (3.1) but with varying values of axial distance x, has been measured at different stations upstream of the two cones existing at distinct values of Reynolds number (figure 15*a*). The interesting feature is that $S(x)$ remains almost uniform upstream of the stagnation point in spite of the important decrease in both azimuthal and axial velocities (figure 15*b*,*c*). In order to understand this, the local parameter $Si(x)$ defined as in (4.1) but with x_0 replaced by x, can be written in the form $Si^2(x) = \frac{1}{2} + (P_\infty - P_1)/\rho V_x^2(0, x)$. In § 2, we have proven that a necessary condition for breakdown is $P_1 = P_\infty$. Hence, at critical, $Si^2(x) = \frac{1}{2}$ everywhere along the streamline on the jet axis. Furthermore, if one assumes a Rankine vortex azimuthal velocity distribution, the above identity leads to $S(x) \approx \sqrt{2}$ for all x. This means that the critical swirl Sc does not depend on selected axial location, provided that it is measured sufficiently far from the stagnation point.

4.5. *Controlling factors for the occurrence of the bubble or cone states*

The bubble and cone have been observed to occur for the same values of the control parameters (Re, S) and for the same nozzle, thereby lending support to the coexistence of bistable states (see state diagrams on figure 11). However, the fact that the domains of existence of the bubble and cone do not coincide for the D_1 and D_2 nozzles (figure 11) may be attributed, to a certain extent, to different flow conditions at the nozzle exit. As seen in figure 14, the profiles of axial and azimuthal velocities are slightly different for the D_1 and D_2 nozzles, especially the axial velocity in the range $0.5 < r/R < 1$.

Moreover, bistability seems to be partly only apparent, another hidden parameter playing a crucial role: our numerous experimental observations strongly support the

https://doi.org/10.1017/S0022112098002870 Published online by Cambridge University Press

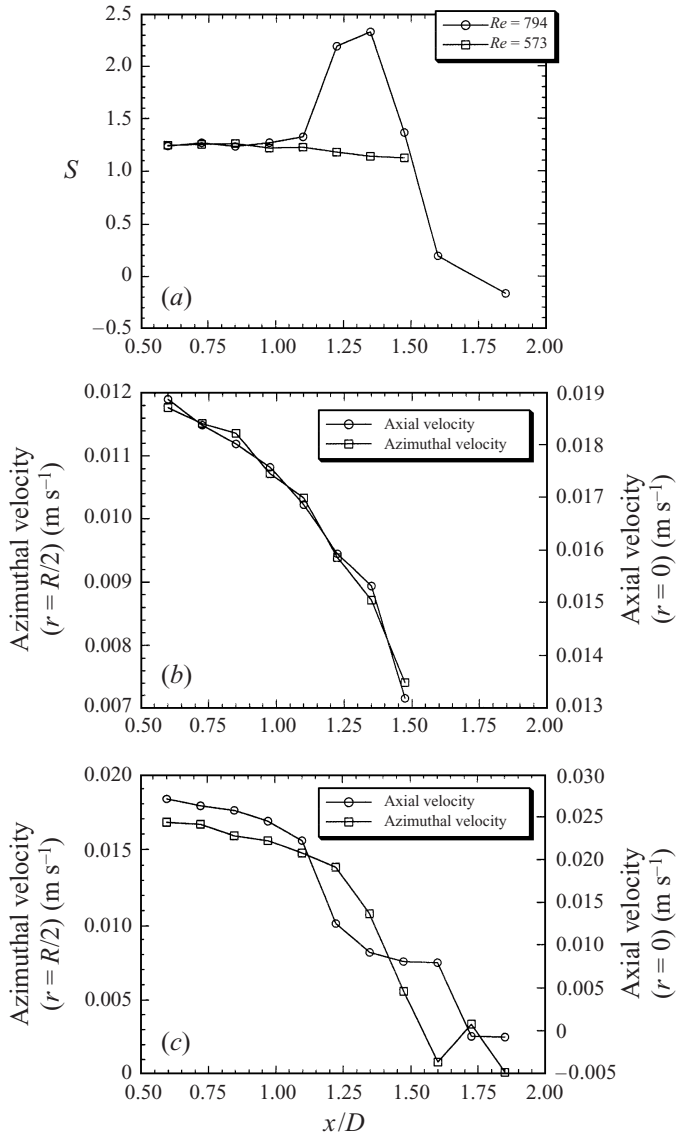


FIGURE 15. (*a*) Local swirl parameter $S(x/D)$ at different axial locations x/D upstream of the two cones existing for $Re = 794$ and $Re = 573$, D_1. (*b*) and (*c*): azimuthal $V_\theta(R/2, x/D)$ and axial $V_x(0, x/D)$ velocities used to estimate the local swirl parameter $S(x/D)$ upstream of the two cones; (*b*) $Re = 573$, $S = 1.29$, (*c*) $Re = 794$, $S = 1.29$.

idea that small temperature inhomogeneities, as small as 0.1°C, have a determining influence on the kind of breakdown which is observed. In our experimental set-up, such small temperature gradients may exist between the jet and the tank, although extreme care was exercised to minimize such differences.

In order to prove the determining influence of temperature, the nature of the observed breakdown state, bubble or cone, was effectively manipulated by purposely adjusting the temperature of the upper constant-head reservoir by a small amount of order 0.1°C. According to our observations, a greater temperature in the jet, relative to the tank, promoted the cone whereas a lower temperature favoured the bubble.

https://doi.org/10.1017/S0022112098002870 Published online by Cambridge University Press

An estimate of the importance of buoyancy effects may be obtained from a simple calculation. For pure water at 20°C, a difference in temperature of 0.1°C between the jet and the tank produces the relative density difference $\Delta\rho/\rho = 2 \times 10^{-5}$. The Richardson number $Ri_1 \equiv \Delta\rho g D_1/(\rho V_x^2)$ based on the nozzle diameter $D_1 = 4$ cm and a jet velocity $V_x = 2$ cm s^{-1} is then equal to $Ri_1 = 0.02$. At first glance, buoyancy effects appear negligible. A more careful reasoning must be carried out that takes into account the peculiar features of the breakdown states. As demonstrated in § 2, one expects the pressure P in the stagnation zone of the cone to be $P = P_\infty$, whereas for the bubble, $P = P_1 \leqslant P_\infty$. One may proceed one step further by examining whether this pressure difference $P_\infty - P_1$ differentiating the bubble from the cone is comparable to the pressure difference induced by buoyancy effects. The Richardson number Ri_2 measuring the relative magnitude of buoyancy forces compared to the pressure difference $P_\infty - P_1$ is defined by $Ri_2 \equiv \Delta\rho g D_1/(P_\infty - P_1) = Ri_1 V_x/\Delta V_x$, where $\Delta V_x/V_x$ is the relative difference of upstream axial velocity between the bubble and the cone. Since $Ri_1 = 0.02$, a relative velocity difference $\Delta V_x/V_x$ of only 2% is sufficient to yield $Ri_2 \approx 1$. Thus the suggested structural difference $\Delta V_x/V_x$ between the bubble and the cone is typically of the same order of magnitude as buoyancy effects generated by a 0.1°C temperature difference. This elementary dimensional argument is seen to account for the extreme sensivity of the selected breakdown state to small temperature inhomogeneities.

We wish to emphasize that the cone is not a spurious state which exists only when a temperature difference is present. This has been proved experimentally at $Re = 575$, by adjusting the temperature so that the jet is colder than the tank by 0.1°C. Buoyancy effects, which seem to promote the cone, are then completely suppressed. A cone is however observed, which demonstrates that this breakdown state exists by itself and not as a result of buoyancy effects.

Furthermore, when no temperature differences are measurable between the jet and the bulk fluid (i.e. below 0.1°C), both states are observed for the same experimental conditions and within a 10 mn time interval. These experimental observations demonstrate that the bubble and cone are two distinct states and not a single state modified by temperature inhomogeneities. This conclusion is strongly corroborated by the fact that there is always a clear distinction between bubble and cone and that no intermediate or 'hybrid' states have been observed. These observations suggest also that a multiple state domain is likely to exist in (Re, S) parameter space, but it is 'blurred' by the high sensitivity of the breakdown states to small temperature inhomogeneities present in our apparatus.

5. Dynamical features

This section is devoted to a description of the typical evolution of the geometrical swirling jet shape as the swirl parameter S is slowly increased from zero to the breakdown threshold Sc while the Reynolds number is kept constant. We do not seek to give a comprehensive description in the entire parameter range below Sc, but only to present how breakdown arises and from which configuration it emerges. A detailed study of the regime $S < Sc$ is postponed to future experiments.

5.1. *Helix configuration*

The main effect of increasing the rotation rate from zero is to enhance the development of helical disturbances and to distort the swirling jet into a steady helix configuration until breakdown occurs. Figure 16 presents a flow visualization of the swirling

https://doi.org/10.1017/S0022112098002870 Published online by Cambridge University Press

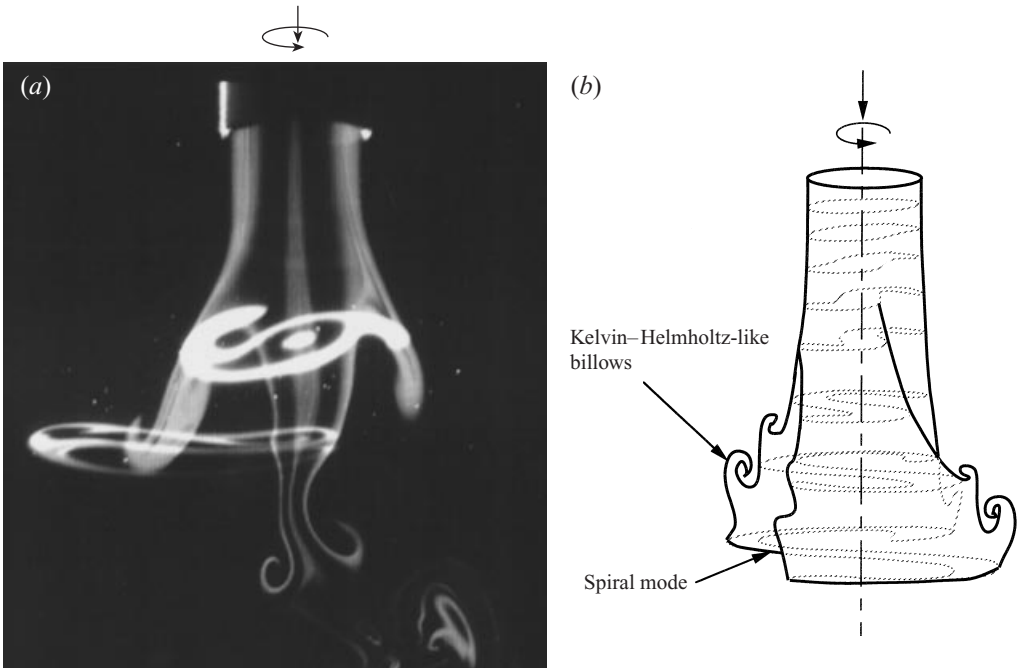


FIGURE 16. (*a*) Flow visualization of helix configuration for $Re = 606$, $S = 1.41$, D_2. Two laser sheets are simultaneously produced in a meridional plane and in a slanted plane from the horizontal. The horizontal laser sheet reveals the spiral shape of the swirling jet which accounts for the 'trident' pattern observed in a meridional plane passing through the jet axis. See remark in caption of figure 6 regarding the evaluation of Re and S. (*b*) Schematic representation of helix configuration.

jet, together with a schematic interpretation, below breakdown onset for the D_2 nozzle at $S = 1.41$ and $Re = 606$. Visualization is achieved by means of two laser sheets generated in a meridional plane containing the jet axis and in a slightly slanted horizontal plane. The swirling jet is seen to consist of a steady helix with a spiral two mode, spatially developing in the axial direction and rotating in the same azimuthal direction as the upstream flow. We emphasize that the azimuthal wavenumber is exactly $m = +2$ if one assumes a modal decomposition of the form $\exp i(m\theta + kx)$. The step of the helix is about $\frac{1}{8}$–$\frac{1}{4}$ turn over an axial distance of one diameter. In addition, Kelvin–Helmholtz-like† instability induces roll-up of the helix in the streamwise direction, thereby leading to a disorganization of the whole pattern farther downstream. Visualizations indicate that the Kelvin–Helmholtz-like roll-up process does not take place uniformly in the azimuthal direction around the helix.

The swirling jet is observed to take a helical shape in all experimental runs below onset of breakdown, for both the D_1 and D_2 nozzles. For the smaller D_2 nozzle, the $m = 2$ helical mode always prevails in the entire range of Reynolds numbers $300 < Re < 1100$, but it is interesting to note that exploratory experiments performed at the larger Reynolds number $Re = 1690$ have revealed the existence

† The word 'like' is used to stress that it is not strictly speaking Kelvin–Helmholtz instability since the shear is not only axial but also azimuthal. In addition, the jet is rotating and may be subjected to centrifugal instability as discussed in § 9. Similar structures are observed in the absence of swirl in the pure jet flow case.

https://doi.org/10.1017/S0022112098002870 Published online by Cambridge University Press

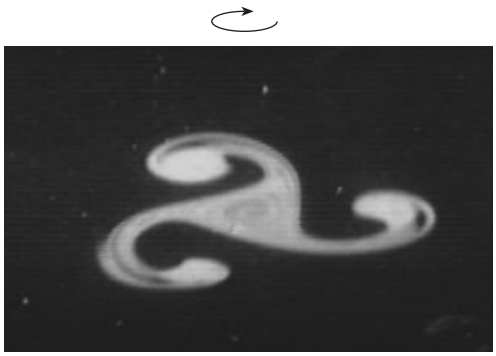


FIGURE 17. Horizontal cross-section of swirling jet for the larger Reynolds number $Re = 1690$, $S = 1.3$, D_2. This Reynolds number is beyond the range of investigation of the present study.

of a well defined $m = +3$ mode below breakdown onset (figure 17). For the larger D_1 nozzle, the $m = 2$ mode is only observed at moderate Reynolds numbers $Re < 750$. For higher Reynolds numbers $750 < Re < 1200$, a complex and unsteady regime prevails which involves a competition between the $m = 2$ and $m = 3$ helical modes. A detailed study of the associated spatio–temporal dynamics has not been attempted.

It should be emphasized that the spatial phase of all helical patterns observed below breakdown onset varies at random from run to run and it is very sensitive to the manner in which the apparatus has been mounted. Such a behaviour indicates that these helical structures are indeed intrinsic to the swirling jet. They are clearly not spurious modes induced by tank confinement effects.

The formation of the helical structure as the swirl parameter S is increased from 0 can be described through a sequence of detailed visualizations for the D_2 nozzle at $Re = 633$ (figure 18). When $S = 0$, the flow has a highly axisymmetric jet configuration which remains laminar down to the bottom of the tank. As S is increased to 0.32 (meridional visualization of figure 18*a*), the swirling jet becomes noticeably unstable at $7D$–$8D$ downstream, with an apparent decrease in diameter. Instabilities develop into billows travelling in the streamwise direction. As shown in the cross-sectional visualizations taken at different axial locations, helical disturbances begin to noticeably distort the swirling jet at $x = 3D$ and they continue to develop gradually along the stream. At $x = 9D$–$10D$, the jet displays a large stationary spiral shape consisting of two distinct arms. For $S = 0.57$ (figure 18*b*, meridional visualization), the instability starts farther upstream and in addition to the apparent decrease in diameter, branching takes place. In the horizontal cross-sections, the swirling jet seems to 'hesitate' between modes $m = 2$ and $m = 3$, and the azimuthal structure remains irregular and unsteady without any clearly identifiable dynamics. When $S = 0.94$ (figure 18*c*), the swirling jet has achieved a fully mature helix configuration. However, the helix suddenly rotates at regular time intervals by half a turn in the same direction as the upstream flow rotation. After each sudden rotation, the phase of the spiral mode appears to remain constant until another rapid turn is initiated. The period of the motion is around 32 s. For both D_1 and D_2 nozzles, this rotational motion of the helix is only observed at intermediate values of the swirl. For larger swirl (figure 18*d,e*), the helix remains perfectly steady, except for the presence of travelling Kelvin–Helmholtz-like billows. As S is increased closer to the breakdown threshold, the spiral structure appears further and further upstream until it reach $x = 1D$. When $S = 1.17$ (figure 18*d*), the

https://doi.org/10.1017/S0022112098002870 Published online by Cambridge University Press

https://doi.org/10.1017/S0022112098002870 Published online by Cambridge University Press

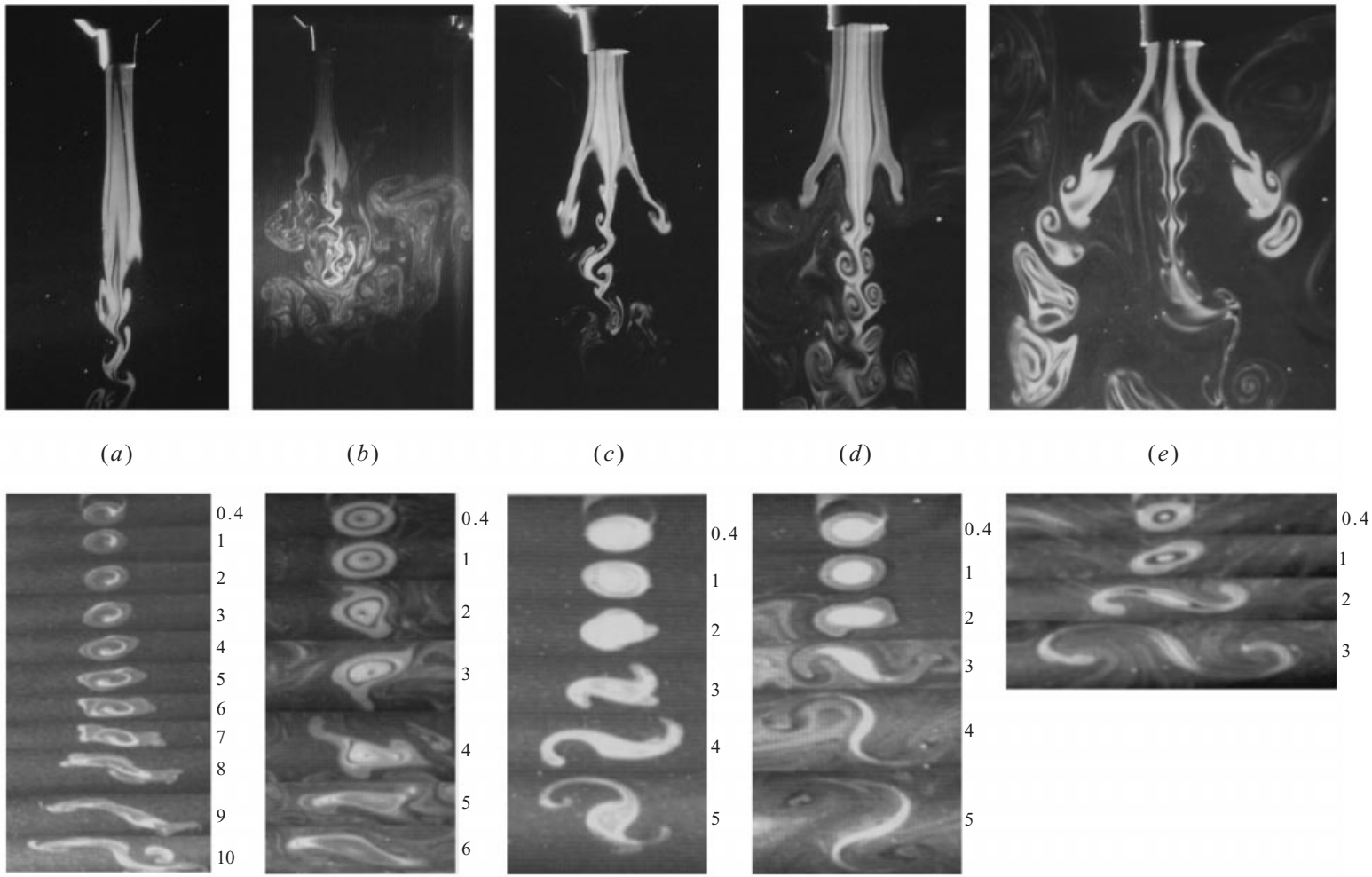


FIGURE 18. Meridional (top) and horizontal (bottom) cross-section visualizations of swirling jet for $Re = 633$, D_2 and increasing values of S: (*a*) 0.32, (*b*) 0.57, (*c*) 0.94, (*d*) 1.17, (*e*) 1.42. Numbers on the left of horizontal cross-sections refer to axial distance from nozzle exit expressed in diameter length.

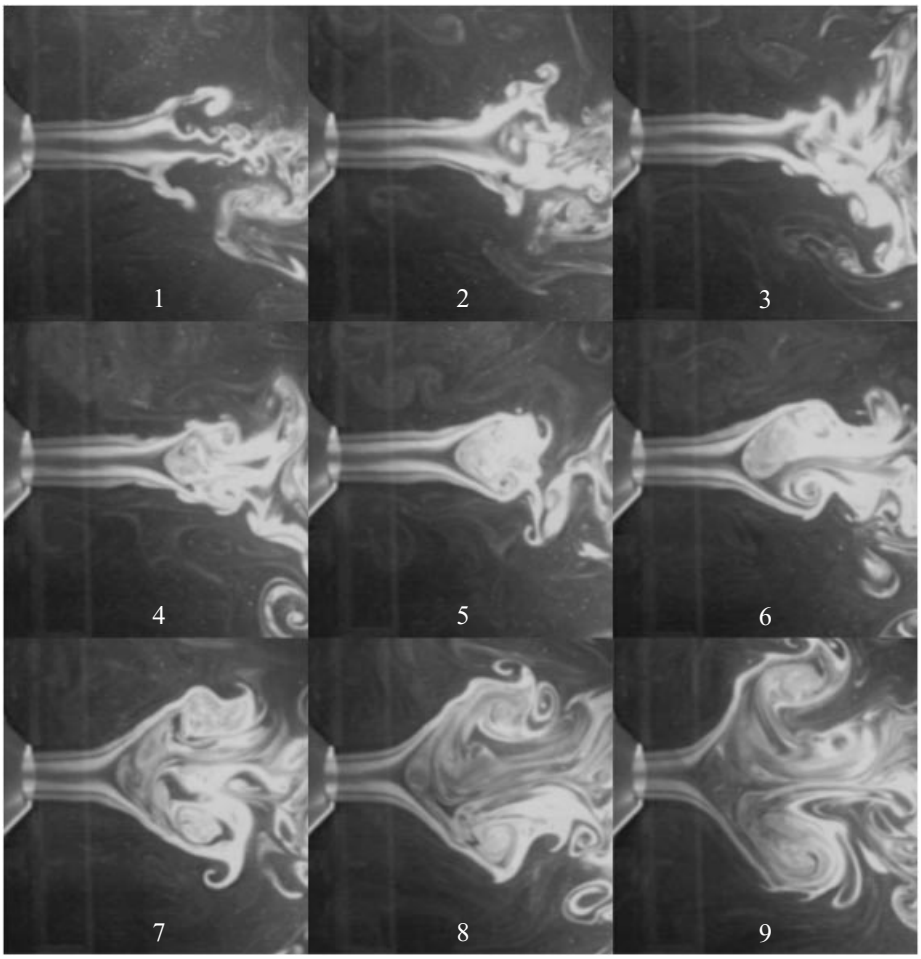


FIGURE 19. Time sequence of events leading to the formation of a cone at 30 s time intervals; $Re = 723$, $S = 1.33$, D_1.

spiral mode $m = 2$ appears at the station $x = 2D$–$3D$, as evidenced in the horizontal cross-sections, whereas, when $S = 1.42$ (figure 18*e*), the same spiral appears abruptly between $x = 1D$ and $x = 2D$.

5.2. *Onset of breakdown*

When the swirl parameter is further increased slightly above the values considered in the preceding section, the helix state give rise to vortex breakdown. For both nozzles, breakdown onset is qualitatively similar but it takes much more time for the D_1 nozzle than for the D_2 nozzle. Characteristic transient times are $T_1 = 6$–10 mn for the D_1 nozzle and $T_2 = 2$–3 mn for the D_2 nozzle. This seems to suggest that the process takes place on a time scale $T \propto D^2$ and that is not affected by confinement effects: the ratio $T_1/T_2 \approx 3$ is of the same order of magnitude as $(D_1/D_2)^2 = 2.6$. As a result of this difference in time scales, the various phases leading to the emergence of breakdown are more distinctly observed for D_1 than for D_2. They are, however, similar and we have therefore chosen to restrict the discussion to the case of the D_1 nozzle.

https://doi.org/10.1017/S0022112098002870 Published online by Cambridge University Press

When S is adjusted slightly below the threshold Sc_a and kept constant, a little bubble, signalling the presence of a transient stagnation point, sometimes appears on the axis of the helix at $4D$ downstream. But this incipient bubble is quickly destabilized and carried away by the Kelvin–Helmholtz-like billows.

When the right value Sc for the onset of breakdown is established, a similar scenario initially occurs, but eventually, a nascent bubble succeeds in 'maintaining' itself within the flow in spite of the surrounding perturbations. As illustrated in the picture sequence of figure 19, this little bubble moves upstream while swelling and being fed by the inner recirculating flow and its probability of survival increases with its size and its proximity to the nozzle exit. The differentiation between bubble and cone takes place in the last stage of upstream migration of the incipient bubble. The bubble can stay forever in a bubble state or, as in figure 19, it may evolve slowly into a cone as a result of internal secondary motion. Note that the characteristic time scales of formation T_1 and T_2 given above are measured from the instant where a permanent bubble is seen in the flow to the full development of the breakdown state.

Any subsequent increase in S above Sc leads to an upstream motion of the breakdown state towards the nozzle exit. This scenario is consistent with earlier descriptions of vortex breakdown onset by Sarpkaya (1971), Escudier (1988) and Brücker & Althaus (1995).

6. Hysteresis phenomena

Hysteretic behaviour at the threshold of breakdown has been confirmed and identified by following the changes in the stagnation point location x/D as the swirl parameter S is increased and then decreased. An example of hysteresis involving the cone is displayed on figure 20. Meridional views of the observed states at different points along the hysteresis loop of figure 20 are also displayed. When S is increased, breakdown arises at $S = Sc_a$ when the equilibrium location of the stagnation point is $X = X_a$ (figure 20). As S is increased beyond Sc_a, x/D decreases, i.e. the stagnation point moves upstream. Conversely, when S is decreased, the stagnation point moves downstream following exactly the same path in (S, X) space as for the increasing case. When S is decreased below Sc_a, breakdown is still observed but the stagnation point is located downstream of X_a. Breakdown only disappears when S decreases down to $Sc_d < Sc_a$, i.e. when the stagnation point moves beyond X_d. Although the hysteresis loop is small in terms of the swirl parameter S, it is undoubtedly of finite extent when measured by the difference $X_d - X_a$. A similar scenario holds for the bubble.

In order to confirm the presence of hysteresis, finite-amplitude perturbations have been imposed on various breakdown states in ranges of Re displaying hysteresis loops. In practice, the perturbations were produced by slightly constricting the flexible exit pipe of the tank with small kicks thereby generating a sharp transient variation of streamwise velocity induced by the resulting pressure wave. When the bubble and cone were perturbed in this manner in the range $S > Sc_a$, sufficiently strong perturbations succeeded in temporarily suppressing breakdown but breakdown ultimately reappeared after a finite time. Metastable breakdown states arising in the range $Sc_d < S < Sc_a$ were also perturbed. For the D_2 nozzle at $Re = 660$, $S = 1.33$, the bubble was successfully swept away by applying appropriate perturbations and it never reappeared within the next half hour. Other perturbations managed to successfully restore the bubble because the associated decrease in streamwise velocity promoted the development of a stagnation zone. A similar experiment was conducted for the metastable cone observed for the D_1 nozzle at $Re = 790$, $S = 1.3$. The cone

https://doi.org/10.1017/S0022112098002870 Published online by Cambridge University Press

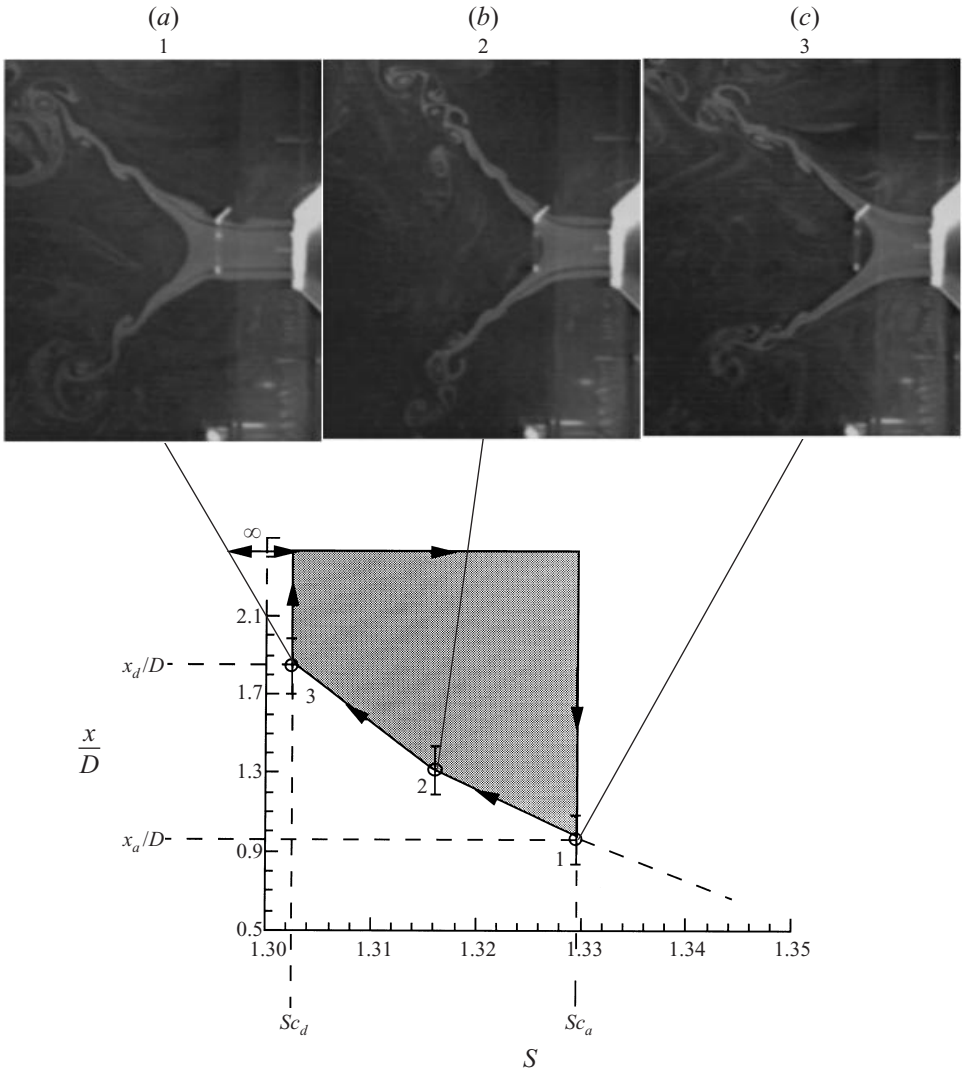


FIGURE 20. Hysteresis loop of a cone in the $(S, x/D)$-plane. x/D denotes scaled axial coordinate of the stagnation point; $Re = 752$, D_1. The pictures show the states observed at each point labelled 1, 2, 3 of the path followed in the $(S, x/D)$-plane.

was suppressed by the application of perturbations and it failed to reappear within the next hour. In contrast with the previous case, external perturbations never succeeded in restablishing breakdown: the little bubble which appeared was always swept downstream before reaching a well developed stage. Further trials led to identical results, thereby indicating that the cone is a state difficult to reach in the metastable range.

7. Axisymmetric nature of vortex breakdown and loss of axisymmetry

The azimuthal structure of the various breakdown states was investigated by means of flow visualization. Horizontal cross-sections of the swirling jet are collected on figure 21 as a function of streamwise distance, for values of S just before breakdown

https://doi.org/10.1017/S0022112098002870 Published online by Cambridge University Press

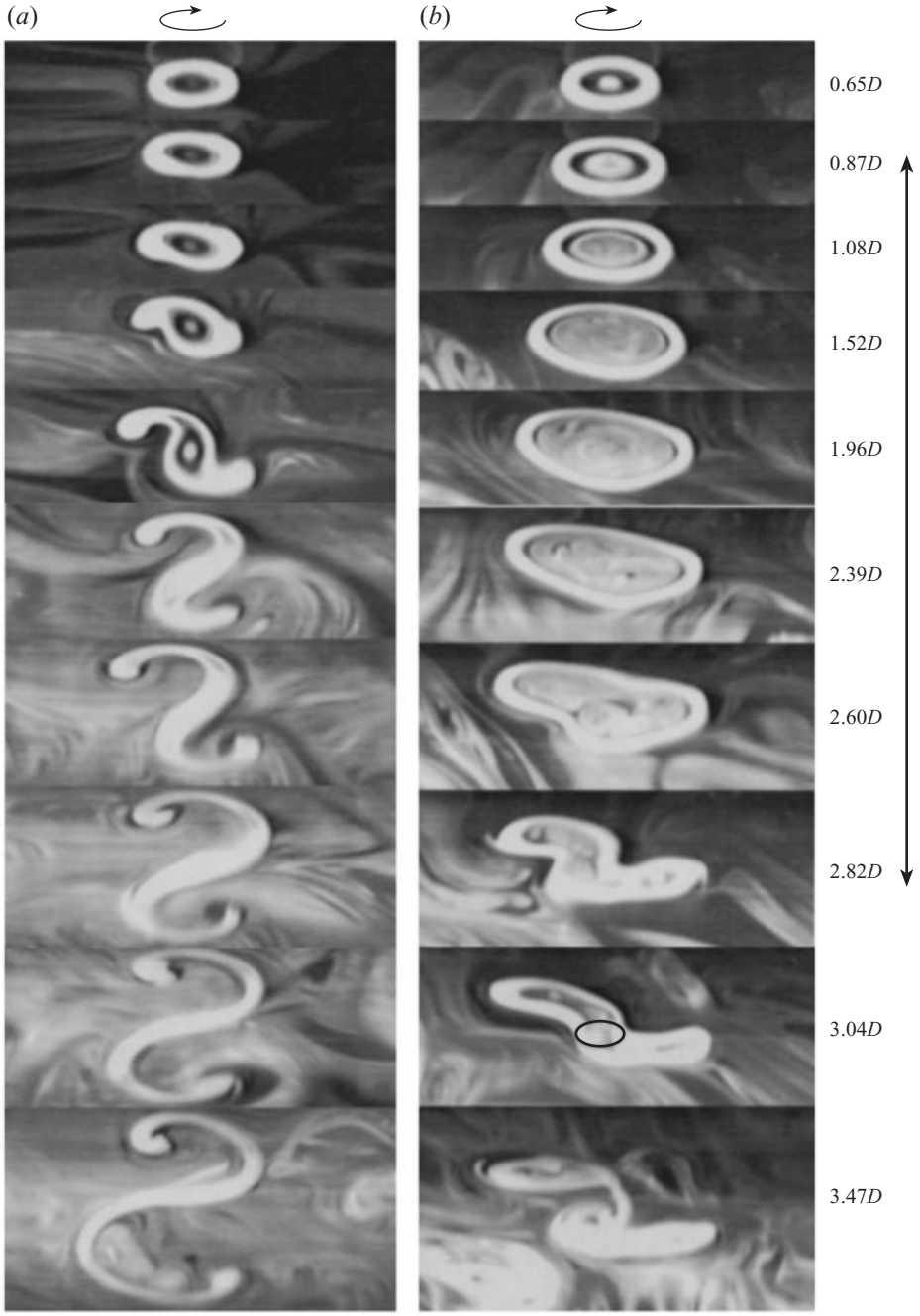


FIGURE 21. Axial evolution of the azimuthal structure at different axial locations below and above breakdown onset. $Re = 606$, D_2. (*a*) Helix, (*b*) bubble. The double arrows indicate the axial extent of the bubble. The circle in picture (*b*) at $3.04D$ identifies the precessing spiral core.

(figure 21*a*) when the swirling jet displays a helical shape and after breakdown when the jet exhibits a bubble (figure 21*b*). According to figure 21, breakdown clearly inhibits the development of helical disturbances to such an extent that the bubble envelope (figure 21*b*) remains axisymmetric much further downstream than the helix

https://doi.org/10.1017/S0022112098002870 Published online by Cambridge University Press

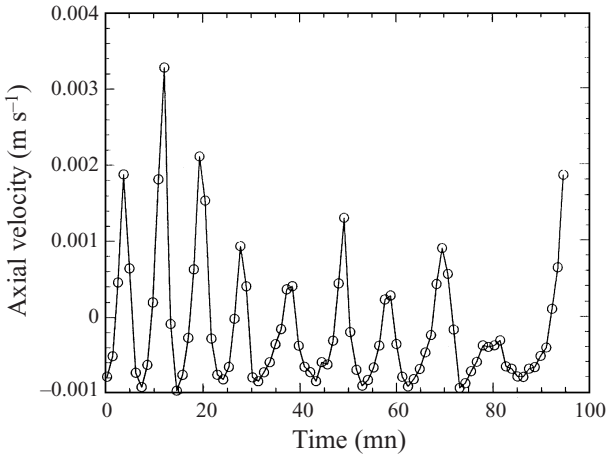


FIGURE 22. Time variations of the axial velocity on the axis of the swirling jet in the vicinity of cone stagnation point; $Re = 656$, D_1.

configuration (figure 21*a*). Helical disturbances only manage to grow in the tail of the bubble and they appear rather suddenly within a short streamwise distance. Such deformations of the rear part of the bubble have already been reported by Faler & Leibovich (1977) and Escudier & Zehnder (1982) under the name 'two-tailed bubble'. In their case it seems to be a separate state from the totally axisymmetric bubble, although bistability and spontaneous change between these two types of bubbles have been reported.

As seen in the cone horizontal cross-section of figure 8, the conical sheet is axisymmetric over its entire extent.

When Re is larger, cone and bubble give way to the asymmetric cone and asymmetric bubble respectively, in which case the stagnation point precesses around the jet axis in a direction similar to the upstream vortex flow. This azimuthal motion can be viewed as a loss of axisymmetry.

8. Temporal dynamics of the cone and the bubble

Recirculating motions produce secondary dynamics of the cone and the bubble which are clearly distinct from the precessing motion of the stagnation point exhibited by the asymmetric cone and bubble. Strong recirculating motions occur within the bubble: the internal region is fed by two counter-rotating vortices and simultaneously flushed through the space between these vortices. This mechanism has been reported in detail by Sarpkaya (1971), Faler & Leibovich (1977, 1978) and Brücker & Althaus (1995) and it is not further discussed here. An additional feature appearing in our experiments is that the core of the spiral tail of the bubble (shown by a circle in the cross-section at $3.04D$ of figure 21*b*) precesses about the swirling jet axis in the same direction as the primary vortex motion. The period of rotation is 11 s for $Re = 582$. Faler & Leibovich (1977) also found that the downstream recirculation zone rotated in the same direction as the primary vortex motion. Unlike Faler & Leibovich (1977), and as in Sarpkaya (1971), the streamwise location of the bubble is observed to remain steady.

In contrast, the oscillations of the cone are slow and affect its whole structure. As mentioned in § 4.1, its oscillatory behaviour is characterized by a regular wandering

https://doi.org/10.1017/S0022112098002870 Published online by Cambridge University Press

motion of the stagnation point along the swirling jet axis accompanied by variations in the opening angle: the cone opens up when the stagnation point moves upstream and vice versa. Temporal variations of the streamwise velocity in the vicinity of the stagnation point (figure 22) demonstrate the regular nature of these oscillations. The amplitude of the stagnation point oscillations decreases as its mean axial location moves closer to the nozzle with increasing swirl. The period mainly depends on the nozzle diameter: $T = 425$–600 s for the D_1 nozzle and $T = 200$–240 s for the D_2 nozzle. The period T approximately scales on D^2 with a slight increasing trend as a function of the Reynolds number.

It should naturally be checked that the observed oscillations constitute an inherent feature of the cone and are not the result of confinement. Confinement may, *a priori*, affect the flow in two different ways: first, it may result from interactions with the tank walls. In this case, the oscillation period should scale as $T \propto L/V_x$, where L is the characteristic dimension of the tank and V_x the mean streamwise jet velocity. Secondly, it may involve an emptying and filling process of a given volume $\mathscr{V}$ at a flow rate $F \propto D^2 V_x$, so that the period scales as $T \propto \mathscr{V}/F \propto \mathscr{V}/(D^2 V_x)$. In this case two scenarii may be envisoned: either the volume $\mathscr{V}$ is independent of nozzle diameter, or it coincides with the volume bounded by the outer cone surface and the tank walls, in which case $\mathscr{V} = \text{const.} - \text{const.} \times D^3$ if the internal volume of the cone is assumed to be proportional to the cube of the nozzle diameter. For any fixed V_x, none of theses scalings can account for the observed increase of the period T with D.

Flow visualizations indicate (figure 23) that the oscillations involve a kind of emptying and filling process of the interior zone. In the successive meridional visualization pictures of figure 23 the dynamics of the cone are followed over one oscillation cycle. The time interval between each frame is not constant in order to show the important phases of the oscillation. The instability of the conical sheet gives birth to several ubiquitous vortices. When the cone is in its most closed configuration, two prominent vortices are generated by the inward rolling up of the conical sheet. In three-dimensional space, these vortices correspond to a toroidal vortex ring trapped within the cone. The pictures on figure 23 demonstrate that the stagnation point moves upstream while the opening angle and the radius of the vortex ring increase. A simple explanation of this phenomenon can be given: according to the Biot–Savart law, the vortex ring induces a counterflow towards the interior of the cone, which contributes to its enlargement and to an upstream displacement of the stagnation point. As the radius of the vortex ring correspondingly increases, the induced velocity in the centre of the internal region weakens and, as a result, the cone closes up again. In the last pictures of figure 23, one can see vortices reappearing on the inner side of the conical sheet that will initiate another oscillation cycle. In addition, flow visualizations have shown that slow recirculating motion exists within the stagnation zone. Indeed, as a result of entrainment by the conical sheet, some internal fluid is advected outside the stagnation zone along the sheet. A reverse upstream motion, made visible by dye tracer, is generated along the axis in order to satisfy mass conservation. Schematically, in meridional cross-sections, two large slowly counter-rotating recirculating eddies are therefore nested in the cone.

In the light of the above discussion, the internal volume of the cone could also have been considered in order to derive a scaling law for the oscillations. But, if $\mathscr{V} \propto D^3$, one obtains $T \propto \mathscr{V}/F \propto D^2/Re$. The period T should decrease with Re which is contrary to observations. The observed scaling law for T remains therefore unexplained.

https://doi.org/10.1017/S0022112098002870 Published online by Cambridge University Press

https://doi.org/10.1017/S0022112098002870 Published online by Cambridge University Press

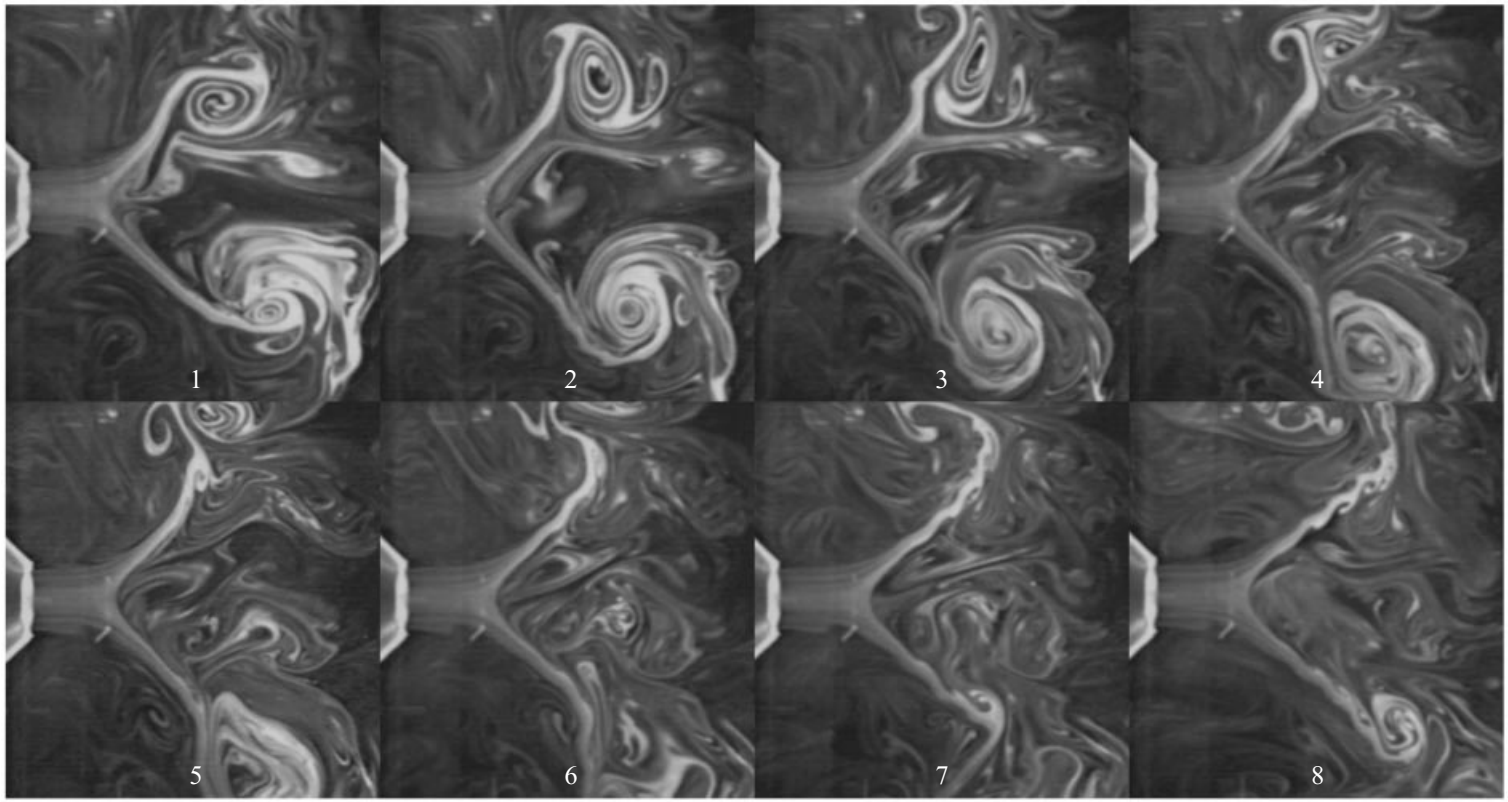


FIGURE 23. Meridional flow visualizations of a cone over one oscillation period T; $Re = 626$, $S = 1.31$, D_1. The time interval between each picture is not constant.

9. Concluding remarks

The vortex breakdown phenomenon has been examined in a swirling jet as a function of the swirl parameter S and the Reynolds number Re. When the swirl parameter S is increased from zero while maintaining the Reynolds number fixed, strong asymmetric disturbances gradually develop to form a steady helix configuration which spatially rotates in the same direction as the upstream flow. As the swirl parameter S reaches the critical value $Sc \approx 1.3$–1.4, independently of the Reynolds number and for both nozzle diameters $D_1 = 40$ mm and $D_2 = 25$ mm, a sudden transition, referred to as vortex breakdown, takes place which is radically distinct from the continuous evolution process observed in the range $0 < S < Sc$: a stagnation point appears in the weakly turbulent region of the swirling jet concurrently with the development of a localized recirculation zone. This structure gradually moves upstream until an equilibrium position is reached. The previous breakdown process can give birth to four distinct configurations, namely the bubble, the cone, the asymmetric bubble and the asymmetric cone. The bubble is similar to the state already observed in confined tubes, whereas the cone does not seem to have been previously identified. The asymmetric bubble, which corresponds to the spiral mode of breakdown, differs from the bubble by the precession of the stagnation point around the jet axis. Finally, the asymmetric cone is a variation on the cone in the same way as the asymmetric bubble on the bubble. Both asymmetric states are observed at large Reynolds numbers. Only the primary configurations, bubble or cone, prevail for $Re \lesssim 800$. Measurable differences in the axial and azimuthal velocity profiles for the D_1 and D_2 nozzles may, to a certain extent, explain the selection between bubble and cone. However, for the same parameter values and for the same nozzle, bubble and cone occur randomly from one experiment to another. The selected state has conclusively been shown to be highly sensitive to minute temperature inhomogeneities as small as $0.1\,^{\circ}\mathrm{C}$: resulting buoyancy forces are sufficient to drive the flow from one breakdown configuration to another.

Breakdown states display hysteretic behaviour: in a range of swirl parameter values $Sc_d < S < Sc_a$, the cone and bubble states are metastable, i.e. stable to infinitesimal disturbances but unstable to finite-amplitude perturbations.

Breakdown is literally akin to a metamorphosis of the swirling jet as evidenced in meridional as well as azimuthal flow visualizations: it inhibits the development of asymmetric disturbances observed when $S < Sc$. Thus, the cone is perfectly axisymmetric and in the bubble the development of helical disturbances is delayed farther downstream. In the light of these results, the asymmetric feature observed in the asymmetric cone and the asymmetric bubble may be interpreted as a secondary breaking of rotational symmetry.

The cone undergoes slow temporal oscillations associated with recirculating motions induced within the internal region. The bubble has been found to remain steady at a fixed station on the jet axis. Its downstream tail precesses around the jet axis in the same direction as the rotation of the upstream flow.

The existence of a cone state supports the view that the essence of vortex breakdown lies in the presence of a stagnation point. This statement is further reinforced by the fact that a simple theoretical argument based on the existence of a stagnation point (§ 2) is capable of predicting the transitional swirl value Sc for breakdown onset.

In closing, it is essential to bear in mind that the basic state generated in the swirling jet configuration intrinsically differs from its counterpart in other experimental set-ups used to study vortex breakdown. The radial variations of $\Gamma(r, x_0) = rV_\theta(r, x_0)$

https://doi.org/10.1017/S0022112098002870 Published online by Cambridge University Press

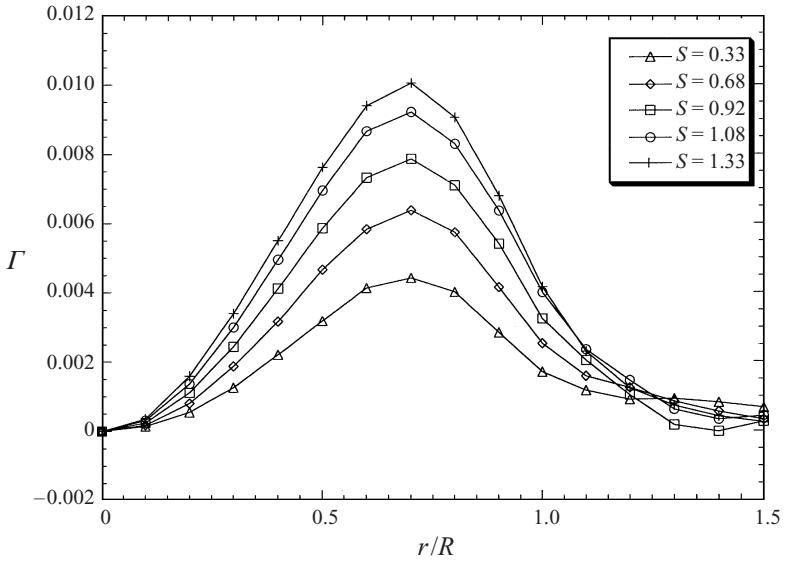


FIGURE 24. Radial variations of circulation $\Gamma(r, x_0) = rV_\theta(r, x_0)$ at $x_0 = 24$ mm, deduced from azimuthal velocity profiles in figure 4(*a*), for different swirl parameter values.

in the upstream swirling jet flow are represented on figure 24 for different swirl parameter values S, as deduced from the azimuthal velocity profiles of figure 4(*a*). The circulation initially displays a parabolic increase away from the axis $r = 0$, as one would expect in solid body rotation. It then reaches a maximum and subsequently decreases to zero for $r > 0.7R$. Thus, the total circulation for large r remains zero since the no-slip boundary condition applies at the outer fixed nozzle wall and no net circulation is thereby produced. This is in sharp contrast with the constant overall circulation prevailing in the Batchelor and Rankine vortex models commonly invoked to study breakdown in trailing line vortices. In the present swirling jet configuration, there exists a finite annular region in which the magnitude of the circulation decreases away from the centre of curvature (figure 24). It remains to be established whether this feature is sufficient to make the flow centrifugally unstable.

This experiment would not have been possible without Ming Ming Wu, Hervé Willaime and Olivier Pouliquen who designed the experiment and performed the qualifying tests. Special thanks go to Antoine Garcia for his technical assistance in setting up the experimental apparatus and to Ivan Delbende for fruitful and stimulating discussions. As always, the joyful spirits of Thérèse Lescuyer played a crucial role in bringing this work to fruition. Enlightening discussions with Tony Maxworthy and Larry Redekopp are gratefully acknowledged. The authors are indebted to the reviewers for many constructive suggestions.

This research was supported by the Direction des Recherches, Etudes et Techniques of the French Ministry of Defense under Grant No. 92-098.

REFERENCES

ALTHAUS, W., BRÜCKER, C. & WEIMER, M. 1995 Breakdown of slender vortices. In *Fluid Vortices* (ed. S. Green), pp. 373–426. Kluwer.

BENJAMIN, T. B. 1962 Theory of the vortex breakdown phenomenon. *J. Fluid Mech.* **14**, 593–629.

https://doi.org/10.1017/S0022112098002870 Published online by Cambridge University Press

Billant, P., Chomaz, J. M. & Delbende I. 1994 Tridents, bubbles and cone-like states in swirling jets. *Bull. Am. Phys. Soc.* **39**, 1921.

Billant, P., Chomaz, J. M. & Huerre P. 1994 L'éclatement tourbillonnaire dans tous ses états. *Let. Assoc. Univ. Mec.* **106**, 3.

Brücker, C. 1993 Study of vortex breakdown by particle tracking velocimetry (PTV). Part 2: spiral type. *Exps. Fluids* **14**, 133–139.

Brücker, C. & Althaus, W. 1992 Study of vortex breakdown by particle tracking velocimetry (PTV). Part 1: Bubble-type vortex breakdown. *Exps. Fluids* **13**, 339–349.

Brücker, C. & Althaus, W. 1995 Study of vortex breakdown by particle tracking velocimetry (PTV). Part 3: Time-dependent structure and development of breakdown–modes. *Exps. Fluids* **18**, 174–186.

Delery, J. M. 1990 Aspects of vortex breakdown. *Prog. Aerospace Sci.* **30**, 1–59.

Escudier, M. P. 1984 Observations of the flow produced in a cylindrical container by a rotating endwall. *Exp. Fluids* **2** 189–196.

Escudier, M. P. 1988 Vortex breakdown: observations and explanations. *Prog. Aerospace Sci.* **25**, 189–229.

Escudier, M. P. & Keller, J. J. 1983 Vortex breakdown: a two–stage transition. *AGARD CP* No. 342 *Aerodynamics of Vortical Flows in Three Dimensions, Paper* 25.

Escudier, M. P. & Keller, J. J. 1985 Essential aspects of vortex breakdown. *Proc. Colloquium on Vortex Breakdown, Feb 11–12, Sonderforschungsbereich 25, 'Wirbelströmungen in der Flugtechnik', RWTH Aachen*, pp. 119–144.

Escudier, M. P. & Zehnder, N. 1982 Vortex-flow regimes. *J. Fluid Mech.* **115**, 105–121.

Faler, J. H. & Leibovich, S. 1977 Disrupted states of vortex flow and vortex breakdown. *Phys. Fluids* **20**, 1385–1400.

Faler, J. H. & Leibovich, S. 1978 An experimental map of the internal structure of a vortex breakdown. *J. Fluid Mech.* **86**, 313–335.

Farokhi, S., Taghavi, R. & Rice, E. J. 1988 Effect of initial swirl distribution on the evolution of a turbulent jet. *AIAA J.* **27**, 700–706.

Garg, A. K. & Leibovich, S. 1979 Spectral characteristics of vortex breakdown flow fields. *Phys. Fluids* **22**, 2053–2064.

Gatsky, T. B. & Spall, R. E. 1991 Numerical studies of vortex breakdown: from helices to bubbles. *Fourth Intl Symp. on Computational Fluid Dynamics*, vol I, pp. 418–423.

Goldshtik, M. A. 1960 A paradoxical solution of Navier-Stokes equations. *Prikl. Mat. Mekh.* **24**, 610–621.

Goldshtik, M. A. 1979 On swirling jets. *Fluid Dyn.* **14**, 19–26.

Grabowski, W. J. & Berger, S. A. 1976 Solutions of the Navier–Stokes equations for vortex breakdown. *J. Fluid Mech.* **75**, 525–544.

Hall, M. G. 1966 The structure of concentrated vortex cores. *Prog. Aerospace Sci.* **7**, 53–110.

Hall, M. G. 1972 Vortex breakdown. *Ann. Rev. Fluid Mech.* **4**, 195–217.

Harvey, J. K. 1962 Some observations of the vortex breakdown phenomenon. *J. Fluid Mech.* **14**, 585–592.

Keller, J. J., Egli W. & Exley J. 1985 Force- and loss-free transitions between flow states. *Z. Angew. Math. Phys.* **36**, 854–889.

Khoo, B. C., Yeo K. S., Lim D. F. & He X. 1997 Vortex breakdown in an unconfined vortical flow. *Expl Thermal Fluid Sci.* **14**, 131–148.

Kopecky, R. M. & Torrance, K. E. 1973 Initiation and structure of axisymmetric eddies in a rotating stream. *Computers Fluids* **1**, 289–300.

Krause, E., Shi, X. & Hartwich, P. M. 1983 Computation of leading edge vortices. *AIAA Paper* 83-1907.

Lambourne, N. C. 1965 The breakdown of certain types of vortex. *Aeronautical Research Council (G.B.), Rep.* ARC–CP–915: NPL–AERO–116.

Lambourne, N. C. & Bryer, D. W. 1961 The bursting of leading-edge vortices: some observations and discussion of the phenomenon. *Aeronautical Research Council R. & M* **3282**, 1–36.

Leibovich, S. 1978 The structure of vortex breakdown. *Ann. Rev. Fluid Mech.* **10**, 221–246.

Leibovich, S. 1983 Vortex stability and breakdown: survey and extension. *AIAA J.* **22**, 1192–1206.

Long, R. R. 1961 A vortex in an infinite viscous fluid. *J. Fluid Mech.* **11**, 611–625.

https://doi.org/10.1017/S0022112098002870 Published online by Cambridge University Press

LUDWIEG, H. 1962 Zur Erklärung der Instabilität der über angestellten Deltaflugeln auftretenden freien Wirbelkerne. *Z. Flugwiss.* **10**, 242–249.

MIKHAIL, M. N. 1979 Optimum design of wind tunnel contractions. *AIAA J.* **17**, 471–477.

PANDA, J. & MCLAUGHLIN, D. K. 1994 Experiments on the instabilities of a swirling jet. *Phys. Fluids* **6**, 263–276.

PECKHAM, D. H. & ATKINSON, S. A. 1957 Preliminary results of low speed wind tunnel tests on a gothic wing of aspect ratio 1.0. *ARC Tech. Rep.* CP Aero. 2504.

SARPKAYA, T. 1971 On stationary and travelling vortex breakdowns. *J. Fluid Mech.* **45**, 545–559.

SARPKAYA, T. 1974 Effect of the adverse pressure gradient on vortex breakdown. *AIAA J.* **12**, 602–607.

SARPKAYA, T. 1995 Turbulent vortex breakdown. *Phys. Fluids* **7**, 2301–2303.

SHTERN, V. & HUSSAIN, F. 1993 Hysteresis in a swirling jet as a model tornado. *Phys. Fluids* **5**, 2183–2195.

SPALL, R. E., GATSKY, T. B. & ASH R. L. 1990 The structure and dynamics of bubble-type vortex breakdown. *Proc. R. Soc. Lond.* A **429**, 613–637.

SPALL, R. E., GATSKY, T. B. & GROSCH C. E. 1987 A criterion for vortex breakdown. *Phys. Fluids* **30**, 3434–3440.

STUART, J. T. 1987 A critical review of vortex-breakdown theory. *Vortex Control and Breakdown Behaviour, 2nd Intl Colloquium on Vortical Flows, Baden, Switzerland, April 6–7, 1987.*

UCHIDA, S., NAKAMURA, Y. & OSHAWA, M. 1985 Experiments on the axisymmetric vortex breakdown in a swirling air flow. *Trans. Japan Soc. Aero. Sci.* **27**, 206–216.

WU, M. M., GARCIA, A., CHOMAZ, J. M. & HUERRE, P. 1992 Instabilities in a swirling water jet. *Bull. Am. Phys. Soc.* **37**, 1789.

https://doi.org/10.1017/S0022112098002870 Published online by Cambridge University Press